

OKINAWA INSTITUTE OF SCIENCE AND TECHNOLOGY
GRADUATE UNIVERSITY

Thesis submitted for the degree

Doctor of Philosophy

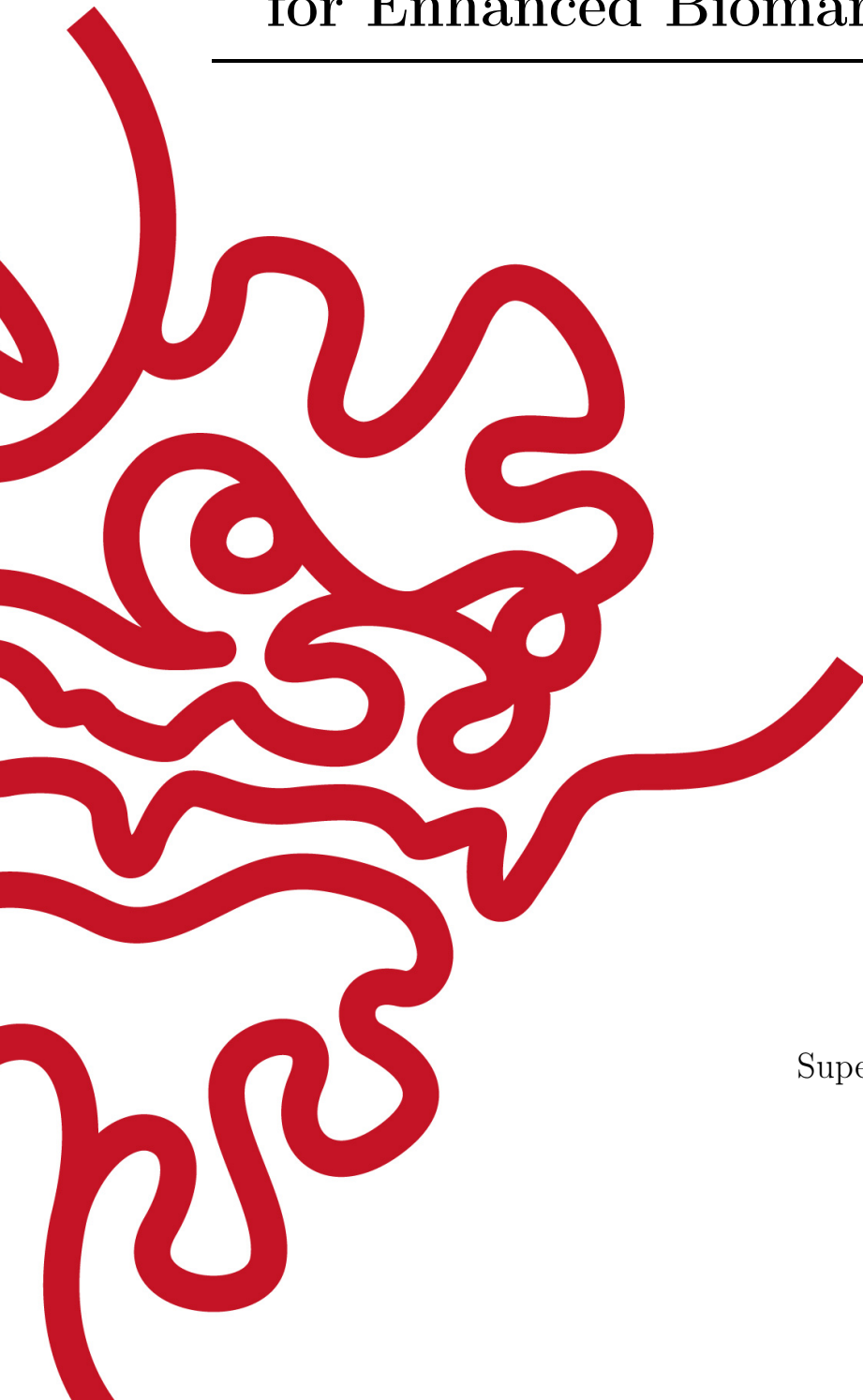
Surface-based Microfluidic Systems for Enhanced Biomarker Detection

by

Shivani Sathish

Supervisor: **Prof. Amy Q. Shen**

March 19th, 2021




Declaration of Original and Sole Authorship

I, Shivani Sathish, declare that this thesis entitled *Surface-based Microfluidic Systems for Enhanced Biomarker Detection* and the data presented in it are original and my own work.

I confirm that:

- No part of this work has previously been submitted for a degree at this or any other university.
- References to the work of others have been clearly acknowledged. Quotations from the work of others have been clearly indicated, and attributed to them.
- In cases where others have contributed to part of this work, such contribution has been clearly acknowledged and distinguished from my own work.
- None of this work has been previously published elsewhere, with the exception of the following:
 1. [Shivani Sathish](#), Kazumi Toda-Peters, and Amy Q. Shen. "Proof-of-concept modular fluid handling prototype integrated with microfluidic biochemical assay modules for point-of-care testing." *View 1.1* (2020): e1. [1]
 2. [Shivani Sathish](#), Noriko Ishizu, and Amy Q. Shen. "Air plasma-enhanced covalent functionalization of poly(methyl methacrylate): high-throughput protein immobilization for miniaturized bioassays." *ACS Applied Materials & Interfaces*. 11.49 (2019): 46350-46360. [2]
 3. Kazumi Toda-Peters, Amy Q. Shen, [Shivani Sathish](#), Doojin Lee, Casey J. Galvin and Kei Funakoshi. "Integrated system for sampling and processing a liquid suspension" (Okinawa Institute of Science and Technology School Corporation), US Patent number: WO2018216607A1, 2018. [3]
 4. [Shivani Sathish](#)^{*}, Sébastien G. Ricoult^{*}, Kazumi Toda-Peters, and Amy Q. Shen. "Microcontact printing with aminosilanes: creating biomolecule micro- and nanoarrays for multiplexed microfluidic bioassays." *Analyst* 142.10 (2017): 1772-1781. [4] ^{*}Equal contribution.

Date: March 19th, 2021

Signature: 

Abstract

Surface-based Microfluidic Systems for Enhanced Biomarker Detection

The 21st century has seen a surge in the development of point-of-care (POC) testing systems integrated with microfluidic bioassay devices, for portable, fast, and user-friendly disease diagnostics. These systems detect diagnostic biomarkers from a small quantity of the patient’s blood plasma, by exploiting their innate nature to bind to specific receptor molecules. A microfluidic bioassay device is considered to be of “high efficiency” when low biomarker concentrations (1 pM–1 nM) can be detected within a few minutes. This thesis explores the collective influence of surface chemistry, biomarker transport and biomolecular reactions at the microscale, to propose design principles for the development of rapid, sensitive and user-friendly fluorescence-based POC systems.

First, we exploit radio-frequency air plasma to covalently tether receptor proteins within polymethyl methacrylate microfluidic bioassay devices, at high-throughput. Next, these devices are integrated with a palm-sized modular Fluid Handling Device that allows precise mixing, filtration, and delivery of fluids, for subsequent detection of *Chlamydia trachomatis* specific antibodies, with a limit of detection (LoD) of 7 nM within 15 mins, serving as a “proof-of-concept” POC testing device.

Next, biomarker transport-dependent kinetic enhancements in microfluidic bioassay systems are investigated using novel 3D glass devices, where real-time binding events between varying concentrations of fluorescently-labelled receptor and ligand antibodies are analyzed. Combing experimental measurements with scaling analysis, two key control dimensionless parameters are proposed to achieve “rapid” and “sensitive” ligand detection: a local Peclet number Pe_δ that characterizes the balance between local convection and diffusion-driven transport of ligands; and a kinetic Damkohler number ($Da_{kinetic}$) that characterizes the balance between the rates of receptor–ligand binding and convection-driven ligand replenishment. We observe that homogeneous ligand binding can be achieved by decreasing the depletion layer thickness ($< 5 \mu\text{m}$) with enhanced local convection at $Pe_\delta \gg 10^5$. At $Da_{kinetic} \ll 10^{-2}$, we demonstrate that enhanced convective ligand replenishment leads to quenching of transport limitations, thereby enhancing the speed of ligand detection at the molecular limit. Finally, we validate that rapid (detection time of 10 mins) and sensitive (LoD of 11.63 pM) ligand detection can be achieved in microfluidic systems with $Pe_\delta \gg 10^7$ for $Da_{kinetic} \ll 10^{-2}$. With prior knowledge of the kinetic constants, these design principles can be applied to various biomolecular systems, paving way to creating highly efficient POC testing systems in the near future.

Acknowledgment

I would like to express my sincere gratitude to my supervisor Professor Amy Q. Shen for her patient and invaluable support throughout my tenure in the Micro/Bio/Nanofluidic unit. I would like to thank Prof. Shen for her consistent feedback on the experimental design and manuscript development for all of my projects. I am also grateful for her mentoring in my professional development, and for having been given several opportunities to collaborate with fellow unit members, which resulted in 4 additional co-authored publications (not listed in this thesis).

I would like to thank the Japan Society for the Promotion of Science (JSPS) for awarding me with the Monbukagakusho Honors Scholarship (2018–2019), and the JSPS DC2 fellowship [2019–2021, Kakenhi grant number 19J11009] to help me with my thesis research. I would also like to thank Okinawa Institute of Science and Technology Graduate University (OIST) and the OIST "Proof-of-Concept initiative" for their financial support, with subsidy funding from the Cabinet Office, Government of Japan.

I would like to thank all the Micro/Bio/Nanofluidics unit members, past and present, for their valuable feedback on my research during group meetings. I would especially like to thank Dr. Charlotte de Blois and Dr. Francesco del Giudice (Swansea university) for helping me understand the fundamentals of fluid dynamics and chemical engineering, which served as the basis for my PhD thesis. I would like to thank Dr. Atsushi Matsumoto, Dr. Hei Man Leung and Dr. Rameez Iqbal, for their constructive criticism on surface chemistry and for teaching me how to use surface characterization instruments. I would like to acknowledge Dr. Daniel Carlson for helping me troubleshoot numerical simulation related issues. I would like to thank Mr. Kazumi Toda Peters and Dr. Hsieh-Tsai for regularly helping me solve microfabrication and microscopy related problems. I would like to acknowledge my collaborators on past and ongoing projects for the positive learning experience. I am indebted to Mrs. Yuno Kaneshi for her persistent administrative help throughout my six years in this unit. I would like to thank Dr. David Vazquez Cortes, Dr. Vikash Chaurasia and Dr. Stoffel Janssens from the Mathematics, Mechanics, and Materials Unit, for their invaluable support in terms of scientific discussions and instrumentation troubleshooting.

I would like to thank my thesis committee members, Professor Eliot Fried and Professor Yohei Yokobayashi for their insightful comments during my tenure as a PhD student. I would also like to thank my thesis examiners, Professor Andrew deMello and Professor Arben Merkoçi for their valuable time spent on reading and for their insightful and encouraging comments on this thesis. Lastly, I would like to thank my friends and family and for their constant encouragement throughout my roller coaster experience as a PhD student.

Abbreviations

1D	1-dimensional
2D	2-dimensional
3D	3-dimensional
μ CP	microcontact printing
APTES	(3-aminopropyl) triethoxysilane
BS3	bis(sulfosuccinimidyl)suberate
BSA	bovine serum albumin
CAD	computer-aided design
CCD	charge-coupled device
CRP	c-reactive protein
EDC	1-ethyl-3-(3-(dimethylamino)propyl) carbodiimide
FHD	fluid handling device
FITC	fluorescein isothiocyanate
GFP	green fluorescent protein
IgG	immunoglobulin G
IL6	interleukin-6
IPA	isopropyl alcohol
LoD	limit of detection
LoQ	limit of quantification
LoB	limit of blank
LSPR	localized surface plasmon resonance
MOMP	major outer membrane protein
NHS	N-hydroxysuccinimide (NHS)
PBS	phosphate buffered saline
PDMS	polydimethylsiloxane
PMMA	polymethyl methacrylate
POC	point-of-care
QCM	quartz crystal microbalance
RF	radio-frequency
ROI	region of interest
SD	standard deviation
SLE	selective laser induced etching
SPR	surface plasmon resonance
TRITC	Tetramethylrhodamine
UV	ultraviolet

This thesis is dedicated to my late aunt, Manjula
Vishwanath, and to the cozy little island of
Okinawa. I could not have done this without you!

List of Publications

The publications and author contributions are listed in the order of appearance in the main body of this thesis.

1. Shivani Sathish, Noriko Ishizu, and Amy Q. Shen. "Air plasma-enhanced covalent functionalization of poly(methyl methacrylate): high-throughput protein immobilization for miniaturized bioassays." ACS Applied Materials & Interfaces. 11.49 (2019): 46350-46360.

Contributions

S.S conceptualized the research idea, fabricated the microfluidic bioassay devices, performed all experiments (apart from XPS characterization) and wrote the manuscript. N.I. performed the XPS characterization experiments. A.Q.S facilitated the structuring and organization of the research plan and assisted in writing and editing the manuscript.

2. Kazumi Toda-Peters, Amy Q. Shen, Shivani Sathish, Doojin Lee, Casey J. Galvin and Kei Funakoshi. "Integrated system for sampling and processing a liquid suspension" (Okinawa Institute of Science and Technology School Corporation), US Patent number: WO2018216607A1, 2018.

Contributions

K.T.P conceptualized the project, designed and fabricated the fluid handling device and microfluidic devices. A.Q.S facilitated the conceptualization of the research plan and assisted in guiding the experimental workflow. S.S. was responsible for the development and characterization of the microfluidic bioassay modules by exploiting microcontact printing. D.L, C.J.G and K.F assisted in experiments that aided the development of the technology. C.J.G and A.Q.S wrote and processed the patent application with proof-reading assistance from K.T.P, S.S, D.L and K.F.

3. Shivani Sathish, Kazumi Toda-Peters, and Amy Q. Shen. "Proof-of-concept modular fluid handling prototype integrated with microfluidic biochemical assay modules for point-of-care testing." View 1.1 (2020): e1.

Contributions

S.S designed the research plan for the biochemical experiments, performed the biochemical assays and characterizations, and wrote the manuscript. K.T.P initiated the project, designed and fabricated the fluid handling device and microfluidic devices and proof-read the manuscript. A.Q.S facilitated the conceptualization of the research plan and assisted in writing and editing the manuscript.

4. Shivani Sathish^{*}, Sébastien G. Ricoult^{*}, Kazumi Toda-Peters, and Amy Q. Shen. "Microcontact printing with aminosilanes: creating biomolecule micro- and nanoarrays for multiplexed microfluidic bioassays." *Analyst* 142.10 (2017): 1772-1781.
^{*} Equal Contribution.

Contributions

S.S designed and fabricated the microfluidic devices and microcontact printing stamps, performed all experiments reported in this paper and wrote the manuscript. S.G.R initially proposed the general research outline and performed preliminary tests (not reported in the manuscript), and assisted in writing the manuscript. K.T.P assisted in the design and fabrication of the microfluidic devices and microcontact printing stamps. A.Q.S assisted in the development of the research plan and assisted in writing the manuscript.

Contents

Declaration of Original and Sole Authorship	iii
Abstract	v
Acknowledgment	vii
Abbreviations	ix
List of Publications	xiii
Contents	xv
List of Figures	xvii
List of Tables	xix
Introduction	1
1 “Air plasma-enhanced covalent functionalization of poly(methyl methacrylate): high-throughput protein immobilization for miniaturized bioassays”	
<i>(Originally published as [2])</i>	11
1.1 Introduction	11
1.2 Published Article	12
1.3 Conclusions	12
2 “Proof-of-concept modular fluid handling prototype integrated with microfluidic biochemical assay modules for point-of-care testing”	
<i>(Originally published as [1])</i>	13
2.1 Introduction	13
2.2 Published Article	13
2.3 Conclusions	14
3 “Microcontact printing with aminosilanes: creating biomolecule micro- and nanoarrays for multiplexed microfluidic bioassays”	

	<i>(Originally published as [4])</i>	15
3.1	Introduction	15
3.2	Published Article	15
3.3	Conclusions	16
4	Kinetic Enhancement of Receptor–Ligand Interactions in Modular Glass Microfluidic Bioassay Devices (<i>Unpublished</i>)	17
4.1	Introduction	17
4.2	Experimental	18
	4.2.1 Fabrication of two-part modular 3D microfluidic bioassay devices	18
	4.2.2 Immunoglobulin (IgG) bioassay using the assembled 3D modular microfluidic device	19
	4.2.3 Image processing and analysis	20
4.3	Theory	21
	4.3.1 Defining the region of interest in the microfluidic system	21
	4.3.2 Estimating the flow field in the confinement region	22
	4.3.3 Mass transport	24
	4.3.4 Receptor–ligand reaction kinetics	24
	4.3.5 Scaling analyses	25
4.4	Numerical Simulation	28
4.5	Results and discussion	29
	4.5.1 Defining local Peclet number (Pe_δ) to characterize ligand transport in the 3D microfluidic channels	29
	4.5.2 Homogeneous binding of ligands across reaction site at high Pe_δ	31
	4.5.3 Uniform ligand flux across reaction site at high Pe_δ	34
	4.5.4 Estimating the kinetic constants of the receptor–ligand IgG reaction	36
	4.5.5 Re-examining the Damkohler number (Da) using kinetic scaling analysis	37
	4.5.6 Development of glass microfluidic bioassay devices with enhanced ligand detection speed and sensitivity	41
	4.5.7 Collective influence of Pe_δ on receptor–ligand reaction kinetics .	43
4.6	Conclusions	45
	Conclusion	47
	Bibliography	51

List of Figures

1	Schematic of a point-of-care (POC) device	1
2	Schematic of a surface-based microfluidic bioassay device	2
3	Schematic of the microcontact printing process	5
4	Illustrative overview of the thesis	9
4.1	Computer-aided design (CAD) model of the modular microfluidic device	19
4.2	Assembly of 3D modular microfluidic bioassay device	20
4.3	Schematic of the microchannel cross section	22
4.4	Schematic of the confinement region with labelled boundaries	23
4.5	Image demonstrating the mesh quality of the COMSOL model	28
4.6	Ligand transport through the 3D microfluidic channel	30
4.7	Influence of Pe_δ on homogeneity of ligand binding across reaction site .	32
4.8	Relationship between Pe_δ and δ as observed by numerical simulations .	35
4.9	Ligand–receptor binding kinetics	37
4.10	Ligand–receptor binding described by kinetic scaling analysis	39
4.11	Influence of Pe_δ on limit of detection of ligand IgGs	42
4.12	Influence of Pe_δ on kinetic constants	44

List of Tables

4.1	Dimensions and flow rates used in the 3D microchannel, shown in Figure 4.3	21
4.2	Operational parameters employed in this study	25
4.3	Damkohler numbers employed in this study	38
4.4	Kinetic constants observed at variable Pe_δ	45
4.5	Dimensionless parameters employed in this study	46

Introduction

Point-of-care disease diagnostic systems

The emphasis on early disease diagnosis and treatment has spurred the development of new technologies aimed at creating faster, reliable and affordable disease diagnostic systems. While economically developed countries are known to be more open to adopting new technologies, resource-limited countries still rely on obsolete technologies due to the low economic stability, and lack of infrastructures and trained personnel. To address these challenges, point-of-care (POC) devices are being developed to serve as cheap, portable, user-friendly, yet reliable disease diagnostic platforms for a wide variety of diseases ranging from metabolic to infectious diseases [5–7].

The versatility of the POC systems enables their use in different environments, to detect a wide range of disease “biomarkers” for both diagnostic and disease monitoring applications. Here, the “biomarkers” are typically proteins, chemical analytes or metabolic markers present in a patient’s blood, saliva or urine, that are indicative of the patient’s health. These biomarkers exist at homeostatic concentrations under normal conditions, while their concentrations fluctuate from these levels when the patient is afflicted with a disease. Disease diagnosis can be performed by first isolating

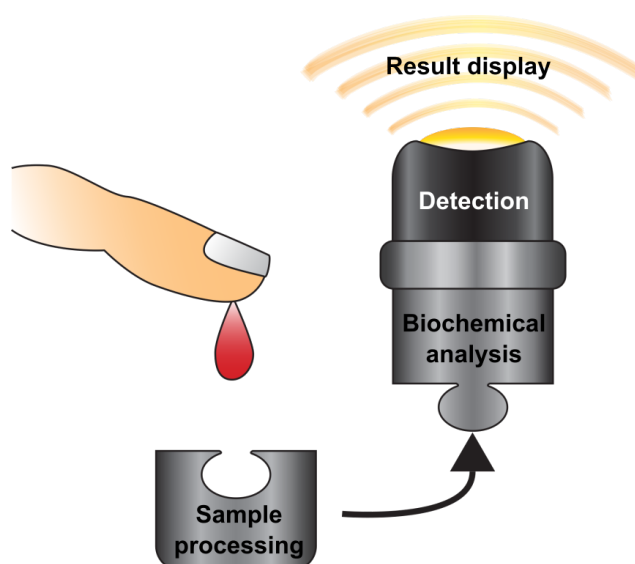


Figure 1: Schematic of a point-of-care (POC) device. Illustrative description of the components of a typical POC device that is capable of processing a biological fluid sample (e.g., blood), perform biochemical analysis to detect diagnostic biomarkers and display the results, in an integrated platform.

and purifying the biofluid sample, and then detecting the presence or absence of the disease-specific biomarkers in the biofluid [8–10].

Typically, POC systems are designed to serve as all-inclusive platforms capable of processing the biofluid samples, performing biochemical analysis to detect the biomarkers in the processed fluid, and display the detection results (Figure 1), within a short period of time, typically within 30–60 mins [11]. While the portability and speed of the integrated systems are attractive features, the adoption of these systems in healthcare facilities is determined by the “sensitivity” and “specificity” of the biomarker detection.

Microfluidic bioassay devices are currently being incorporated into the POC systems for further miniaturization, to allow for the development of rapid yet sensitive and well-controlled biomarker detectors, with limited sample and reagent volume requirements.

Microfluidic bioassay devices

Since the early 1980’s, microfluidic systems have significantly evolved to enable the creation of cheaper, faster and more reliable means for simultaneous biochemical analysis of multiple biomarkers [12–14]. These systems consist of networks of microscale channels that enable enhanced transport of biomarkers in the biofluids for subsequent biochemical reactions with specific capture molecules (Figure 2).

Advances in microfabrication techniques have allowed for the fabrication of microfluidic devices using a wide range of materials. Low-cost poly-(dimethylsiloxane) (PDMS)–glass hybrid devices are generally employed for laboratory scale analysis. These devices are easy to fabricate, optically transparent and allow for detection of

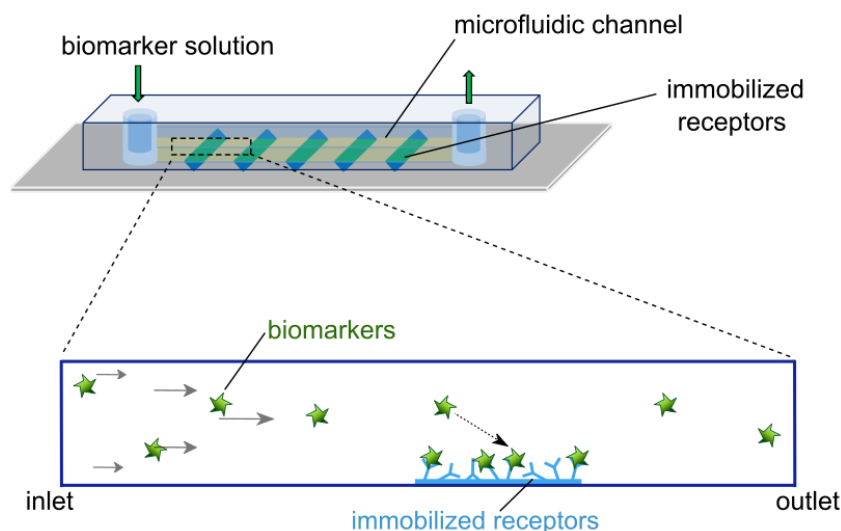


Figure 2: Schematic of a surface-based microfluidic bioassay device. A solution of biomarkers (green stars) are flowed through a microchannel consisting of immobilized receptors (blue sticks) on the bottom wall of the channel. The biomarkers react with the immobilized receptors when in close proximity, to complete the biochemical assay reaction.

biochemical reactions using conventional microscopy techniques. However, the high susceptibility of channel deformation at high flow rates, makes PDMS–glass devices less compatible for fast flows [15, 16]. On the other hand, novel selective laser-induced etching (SLE) processes has allowed for the fabrication of truly 3-dimensional (3D) microfluidic systems embedded in glass substrates [17]. While these systems are able to withstand fast flows and allow for the optical detection of biochemical reactions, they are not amenable to large scale processing. To enable high-throughput fabrication of microfluidic devices with the desired optical traits of the glass-based systems, polymeric substrates such as polymethyl methacrylate (PMMA), polycarbonate, etc., are increasingly employed in POC systems [18, 19].

Irrespective of the material of the microfluidic device, the biofluids are transported through the channels by one of many active fluid delivery processes such as pressure-driven flow, electrokinetic flow, centrifugal flows, or by passive methods such as capillary flow [20]. While different applications benefit from different modes of fluid delivery, pressure-driven flow proves to be the most beneficial for automatized microfluidic bioassay systems, as it enables continuous and sequential delivery of reagents with better control over flow parameters throughout the process [21]. Additionally, flow in these systems is laminar, i.e., the biomarker-rich biofluids are transported in independent parallel layers without mixing. This makes the fluid transport through these systems easy to predict with the help of well-defined analytical models [22]. As a consequence, fast and reagent-friendly microfluidic systems can be designed by simply optimizing those parameters that have a significant influence on the biochemical reaction employed to detect the biomarkers.

Surface-based receptor–ligand bioassays:

The process of detecting biomarkers in a microfluidic bioassay device relies on the biochemical reaction between biomarker ligands and complimentary receptor molecules. Here, the receptor molecules are generally proteins such as antibodies [23], or DNA fragments such as aptamers [24], that are capable of recognizing and binding to specific biomarker ligands. These receptor–ligand recognition reactions are highly specific, thereby enabling the detection of the disease biomarkers with high-specificity.

Surface-based systems are frequently used to perform these biochemical analyses, where the biomarker ligands are flowed in solution through the microfluidic channels coated with receptor molecules on one or more surfaces of the channels (Figure 2). Here, the receptor–ligand reaction occurs on the solid–liquid interface in the microfluidic channel [25]. At the microscale, the ligands are in increasingly close proximity to the channel walls thereby increasing the probability of the receptor–ligand interactions in microfluidic systems. Due to the large surface-to-volume ratios in the microfluidic systems, the speed of the receptor–ligand reaction is enhanced, with drastically reduced reagent volumes required for the entire process [23].

While the geometrical scale of the microfluidic channel plays an important role in the speed of the ligand detection, the sensitivity of the system is determined by the density, biofunctionality and orientation of the immobilized receptors [26].

Surface chemistry for immobilization of receptors:

Receptor immobilization, is the fundamental process that affects the “sensitivity” of the surface-based microfluidic bioassay systems. For this purpose, different surface functionalization strategies have been proposed depending on the material used to fabricate the microfluidic devices. The common goal of all the functionalization strategies is to enable covalent immobilization of the receptor molecules, such that the receptors are able to withstand the high flow rates experienced on the channel walls. Most commonly employed covalent immobilization strategies are based on coupling chemistries that initiate an amide bond ($CONH$) between amine (NH_2) and carboxylic acid ($COOH$) moieties [27, 28]. Of the available coupling chemistries, two of the most commonly used chemistries are (i) 1-ethyl-3-(3-dimethylaminopropyl) carbodiimide (EDC), N-Hydroxysuccinimide (NHS) chemistry, and (ii) bis(sulfosuccinimidyl)suberate (BS3) chemistry. EDC is a carbodiimide that reacts with the $COOH$ groups either present on biomolecule surfaces [28], or on the material surface, to form a highly reactive ester intermediate. This ester then reacts with the available NH_2 groups on the substrates, or biomolecule surfaces to form the final amide bond. Here, NHS is used to stabilize the ester during the conjugation process [29]. Conversely, BS3 is an amine to amine [NH_2 to NH_2] crosslinker [30] which is a water soluble analog of NHS.

Regardless of the functionalization strategy, utmost care must be taken to ensure that the surface manipulations do not disrupt the conformations of receptors [31]. In addition, the surface coverage or density of the receptors has shown to be another key parameter that influences the receptor–ligand reaction efficiency [32].

Existing techniques used to pattern biomolecules on glass and polymeric surfaces at the micro- and nanoscales, include physical patterning approaches such as photolithography [33], adsorption of biomolecules confined to microfluidic networks [34], and colloidal lithography [35]. These techniques are either plagued by high costs, low throughput, or have limited control over the geometry and functional properties of the immobilized receptors.

Microcontact printing:

On the contrary, microcontact printing (μ CP) [36–38] has been preferentially used to immobilize biomolecules in well-defined patterns on a wide range of substrates. During this process, a liquid solution containing receptor molecules are inked on micropatterned elastomeric PDMS stamp surfaces. After incubation, the stamps are washed, dried and stamped onto a substrate with higher surface energy than that of the stamp (Figure 3). This causes the transfer of the inked molecules from the stamp to the substrate.

Although these microcontact printed biomolecules have been successfully incorporated into microfluidic devices [39, 40], several challenges remain. First, as patterned biomolecules are physically adsorbed onto the surfaces driven by hydrogen-bonding and van der Waals forces [41], they are unable to withstand high shear stresses introduced by the flow present in microfluidic channels. As a result, it gives rise to gradual desorption and degradation of patterned biomolecules that lead to reduced device performance and poor shelf life. Secondly, since partial dehydration of biomolecules is a prerequisite to the μ CP technique, the probability of protein denaturation and impaired biological

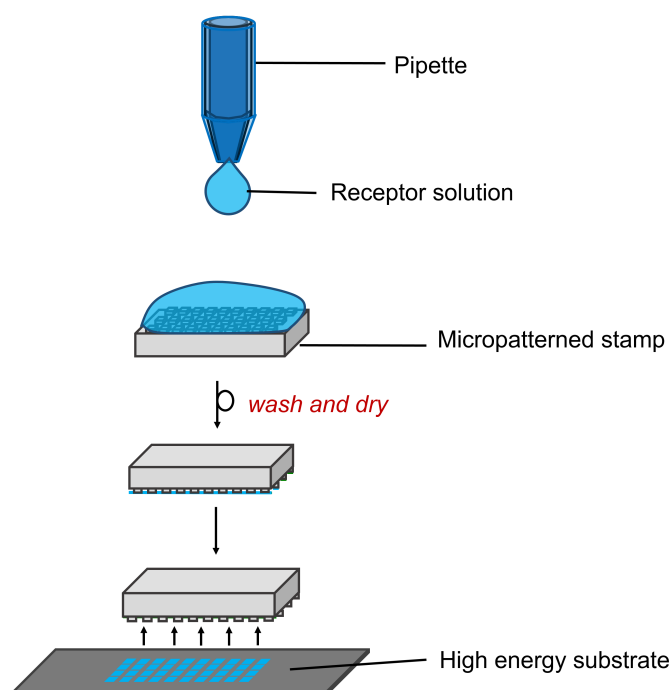


Figure 3: Schematic of the microcontact printing process. A receptor solution is deposited on a micropatterned PDMS stamp. The incubated stamp is washed and dried before transferring the receptors via stamping onto a higher energy substrate.

activity is high. Lastly, patterning a substrate with multiple biomolecules proves to be difficult and time-consuming, as each individual stamp can only be utilized to pattern a single ink at a time.

Nevertheless, there is immense potential to incorporate microcontact printing for patterning surfaces with linkers such as silanes [42], that enable subsequent coupling of biomolecules. This ensures the preservation of biomolecule functionalities, with the added advantage of covalent coupling to surfaces which enable biomolecules to withstand the high flow rates in the surface-based microfluidic devices.

Fluorescence-based detection:

Following receptor immobilization, the microfluidic bioassay system is primed to capture biomarker ligands from the biofluid. However, suitable detection methods are required to detect the receptor–ligand reactions occurring in the systems. The commonly employed detection methods are holistically divided into two families: (i) label-free and (ii) label-based detection strategies [43]. Label-free strategies rely on the direct detection of receptor–ligand reactions occurring on metallic thin films or nanostructure, by monitoring the changes in surface mass adsorption. The most commonly used label-free detection strategies rely on optical sensing of mass dependent surface electron resonance energy changes using surface plasmon resonance (SPR) and localized surface plasmon resonance (LSPR) sensors [44–46], or direct detection of mass

variation using quartz crystal microbalance (QCM) [47, 48]. While these sensors have been shown to be highly sensitive to detect small changes in concentrations, they require complex instrumentation making it difficult to integrate within a microfluidic chip.

On the other hand, more conventional label-based detection strategies such as colorimetric detection [49] and fluorescence detection [50], rely on commonly used imaging instruments such as absorbance readers and microscopes. Owing to the ease of integration with microfluidic bioassay systems, fluorescence-based detection has been the preferred detection strategy, both at the laboratory and industrial settings. Using this strategy, the receptor–ligand reactions are detected with the help of tertiary fluorescently-labelled detection molecules that are specific to the ligands. In a typical fluorescence-based surface bioassay, the fluorescently-labelled detection molecules are flushed through the channels after the receptor–ligand reaction is completed. Subsequently, the changes in fluorescence intensity are monitored via fluorescence microscopy. Here, the fluorescence intensity is proportional to the concentration of ligands captured in the bioassay system, based on the Beer-Lambert law [51]:

$$F = kI_0\phi[1 - (10^{-\epsilon bc})], \quad (1)$$

where, F is the fluorescence intensity, k is the proportionality constant related to the instrument, I_0 is the intensity of incident light, ϕ is the fluorescence quantum yield, ϵ is the molar absorptivity of the molecule (L/mol.cm), b is the path length and c is the concentration of the molecule (moles/L). In typical fluorescence-based bioassays, dilute solutions of fluorescently-labelled detection molecules are employed. As a consequence, it is assumed that only <2% of the excitation energy is absorbed, resulting in the simplified equation 2:

$$F = kI_0\phi\epsilon bc. \quad (2)$$

This relationship that shows that the analyte concentration is proportional to the fluorescence intensity, serving as the foundation of quantitative analyses in fluorescence-based bioassays.

Kinetic enhancements:

While the “sensitivity” of the microfluidic bioassay systems is determined by the biofunctionality of the immobilized receptors, the “biomarker detection speed” is influenced by the operational and geometric characteristics of the device. Several previous studies have demonstrated that mass transport limitations are common problems observed in surface-based bioassay devices [26]. These limitations arise when the ligands are depleted from the solution by the receptor-coated surface, at a rate faster than the rate at which the ligands are replenished by the flowing solution.

Several reports have indicated that receptor–ligand reaction kinetics can be enhanced using microfluidic bioassay systems as a result of the reduced length scales. Specifically, authors have reported the influence of several microfluidic operational and geometric variables on the ligand detection speed. Ekins *et. al.*, showed that the ligand capture rate increased significantly with decreasing size of the reaction site [52].

Several following reports corroborated these observations, proving a proportional relationship between the size and geometry of the reaction sites containing the immobilized receptors and the receptor–ligand reaction kinetics.

In parallel, the aspect ratio of the microfluidic channels was shown to significantly influence the receptor–ligand kinetics. Specifically, authors demonstrated that microfluidic channels with rectangular cross-sections resulted in faster ligand detection rates when compared to square microchannels [53]. Additionally, Lynn *et. al.*, showed that the efficiency of ligand capture in microfluidic systems scales inversely with the microchannel height [54].

These experimental observations of receptor–ligand reaction kinetic enhancements in microfluidic bioassay devices were explained to be a consequence of modified ligand transport to the reaction site, resulting from the combined effect of length scale reduction at micron and sub-micron scales, and enhanced ligand transport in these systems.

With the help of scaling analyses, well-established analytical models have attempted to encapsulate various inter-dependent variables into several dimensionless parameters to provide order-of-magnitude comparisons between competing phenomena, i.e., convection, diffusion and reaction. Depending on the rate-limiting time scale, the microfluidic devices commonly operate in convection-limited, diffusion-limited, or reaction-limited regimes. Diffusion-limitations are commonly observed in static and high flow rate microfluidic systems, where the biomarker detection time is purely determined by the time taken for the biomarker molecules to diffuse to the receptor-coated surfaces [55, 56]. On the other hand, convection-limitations are commonly observed in nanofluidic systems, where the biomarkers are able to diffuse to the receptor-coated surfaces faster than they are convected through the channels, due to reduced length scales [57]. Diffusion and convection-limitations, collectively termed as “mass-transport limitations”, have been described to contribute to the low biomarker detection speeds in surface-based bioassay systems. Current efforts are focused on developing reaction-limited bioassay systems, where the rate of ligand transport to the receptor-coated surface is faster than rate of receptor–ligand reaction. In this desired regime, the biomarker detection speed is solely determined by the innate kinetic properties of the receptor–ligand binding reaction [26].

Researchers have proposed design rules to help engineers develop reaction-limited microfluidic bioassay systems by enhancing convective ligand transport to the receptor-coated surfaces [26, 58, 59]. However, the applicability of these design rules under extremely fast flows is still unclear.

Biomarkers

Green fluorescent protein (GFP):

Green fluorescent protein (GFP) was first isolated from the bioluminescent jellyfish *Aequorea victoria* for its intrinsic property to exhibit green fluorescence when exposed to blue light. This intrinsic fluorescing property is attributed from the ability of the protein to naturally form internal chromophores encapsulated within cylindrical peptide barrels. Owing to the sensitivity of the protein structure to changes in pH, ionic

strength and temperature of the environment, GFP has been extensively exploited in biotechnology applications [60, 61]. Most importantly GFP has served to be beneficial in surface chemistry studies where changes in surface chemistry-mediated protein conformations can be easily monitored by detecting fluorescence quenching due to degeneration of GFP structure. Additionally, fluorescence-based receptor–ligand binding kinetics can be easily monitored without the need for the tertiary fluorescently-labelled molecule, due to the innate fluorescing properties of the GFP molecules.

Immunoglobulin G (IgGs):

When a person is afflicted with a bacterial, viral or fungal infection, the person’s immune system secretes factors called antibodies or immunoglobulins (Ig), to neutralize those pathogens. Depending on the type of infection, various kinds of immunoglobulins such as immunoglobulin A (IgA), M (IgM), G (IgG), etc. are circulated around the body via the patient’s blood. Each Ig has a different role during the process of combating the pathogen. Immunoglobulin G (IgG) is the most common type of antibody, constituting almost 75% of the antibodies in the patient blood. In addition to aiding in the lysis of the invading pathogen, IgGs provide long-term immunity against the pathogen, protecting the patient from further infections. As a result, these molecules have served as prognostic biomarkers, where their detection provides information about the patient’s state of infection and recovery [62].

For example, clinical research has shown that bacterial *Chlamydia trachomatis* infections are the most prevalent sexually transmitted infection in the world [63]. As these infections are asymptomatic, they lead to a continued widespread of the infection. Additionally, this bacterial infection has been identified to cause pelvic inflammatory diseases (PID), infertility and miscarriages in women. Clinicians diagnose these patients by performing antibody tests from the patient blood in order to quantify the IgGs specific to protein fragments of *C. trachomatis*, such as major outer membrane protein (MOMP) [64, 65]. In addition, with the help of genetic engineering, standard IgGs have been fluorescently labelled to allow researchers to study and develop IgG bioassay systems for a wide range of diseases.

Interleukin-6 (IL6) and C-reactive protein (CRP):

Interleukin-6 (IL6) [66, 67] and human C-reactive protein (hCRP) [68, 69] have been known to be the most important biomarkers of neurological, cardiovascular and other pathophysiological conditions that arise from tissue inflammation or infection. Quantitative detection of these biomarkers has immensely helped in early diagnosis and treatment of these diseases. For accurate disease diagnostics, sensitive assays and biosensing technologies are required to reliably detect minute quantities of these biomarkers [8, 70]. In addition, as these molecules have been well-characterized over the years, bioengineers are equipped with detailed molecular information that allows them to fabricate bioassay systems for sensitive detection of CRP and IL6 with the help of complimentary receptor antibodies (proteins) or DNA aptamers.

Thesis outline

The centralized aim of this thesis is to propose design principles for the development of rapid and sensitive point-of-care disease diagnostic platforms. To demonstrate the versatility of the proposed principles, each process discussed in this thesis was tested on a wide range of biomarkers. As illustrated in Figure 4, the thesis is broken down into four chapters, where each process is elaborated as a separate chapter.

In Chapter 1, we present a high-throughput functionalization strategy for the development of polymethyl methacrylate (PMMA) microfluidic bioassay devices. Specifically, we demonstrate the generation of functional *COOH* groups on the surfaces of PMMA using radio-frequency (RF) air plasma. These *COOH* groups subsequently serve as functional sites for covalent adhesion of proteins such as green fluorescent protein (GFP) and major outer membrane protein (MOMP) of *Chlamydia trachomatis*, via 1-ethyl-3-(3-dimethylaminopropyl) carbodiimide (EDC), N-hydroxysuccinimide (NHS) chemistry. The functionalized surfaces are then incorporated into microfluidic devices to enable the detection of clinically significant concentrations of *Chlamydia trachomatis*-specific immunoglobulin G (IgGs).

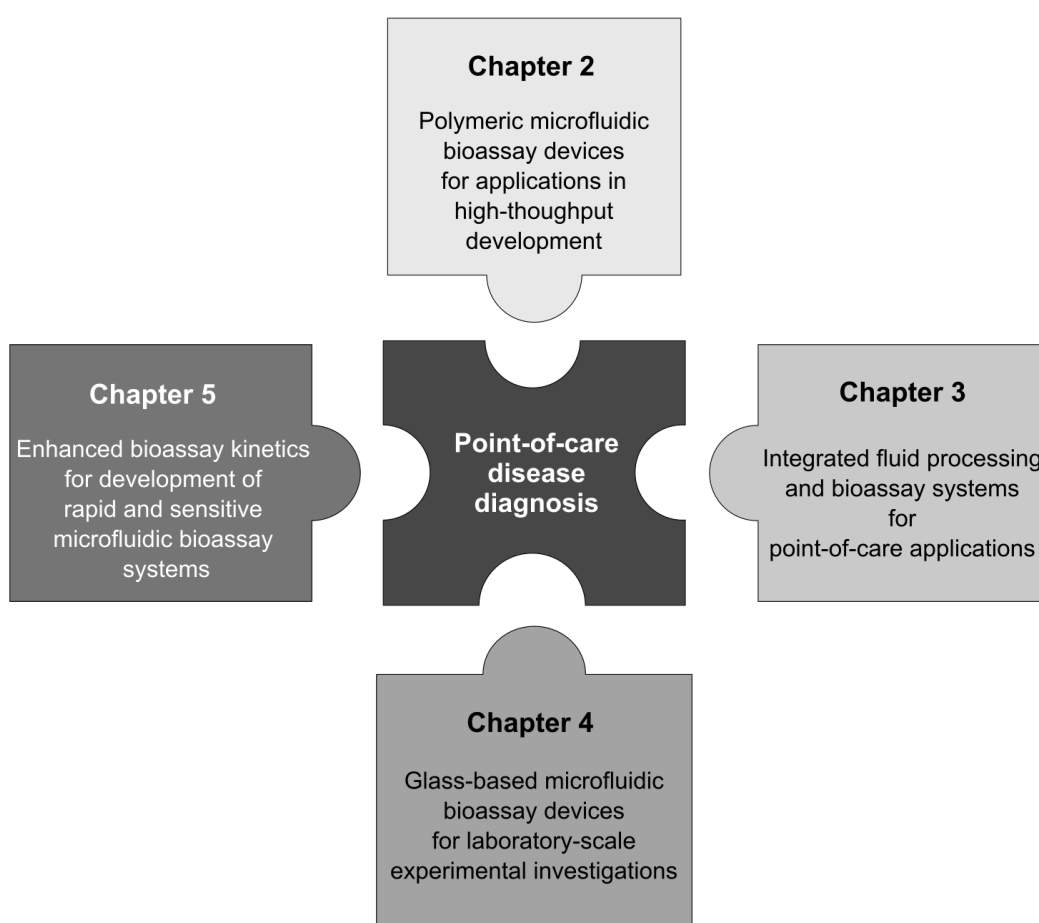


Figure 4: Illustrative overview of the thesis. The thesis is broken down into four distinct chapters that address different experimental steps involved in attaining the centralized goal, i.e., the development of a point-of-care disease diagnostic platform.

These developed PMMA microfluidic bioassay devices are integrated with a novel fluid handling device (FHD) in Chapter 2, to demonstrate a proof-of-concept point-of-care testing device. The integrated module allows for the collection of a fluid sample, mixing with detection antibodies, delivery to the PMMA microfluidic bioassay devices and detection of *C. trachomatis*-specific IgGs via fluorescence microscopy.

To address issues regarding sample volume requirements and sensitivity of the microfluidic device, we then focus on understanding the fundamentals of flow-dependent receptor–ligand reaction kinetics. In Chapters 3 & 4, we employ glass-based microfluidic devices to allow for better control of geometrical and flow parameters in this study. In Chapter 3, we present a microcontact printing enabled bio-functionalization strategy that allows the covalent immobilization of IgGs within glass-based microfluidic devices. The immobilized IgGs retain their ability to capture biomarkers such as C-reactive protein (CRP) and interleukin 6 (IL6), following the immobilization process.

In Chapter 4, this functionalization strategy is used to fabricate robust 3D microfluidic bioassay devices capable of generating high shear flows. These devices are used to investigate the validity of the proposed design design rules that have been used as a universal standard to study microfluidic bioassay systems, since the early 2000's. Specifically, we critically analyze their validity when applied to systems relying on extremely fast flows. First, we re-examine the scaling analyses proposed by the previous models to validate the observed experimental results. Next, we proposed modified design rules to allow for fabrication of fast yet sensitive systems. Finally, we use the new design rules to fabricate devices that enable the detection of a wide range of biomarkers, within 15 mins.

Chapter 1

“Air plasma-enhanced covalent functionalization of poly(methyl methacrylate): high-throughput protein immobilization for miniaturized bioassays” *(Originally published as [2])*

1.1 Introduction

Miniaturized systems, such as integrated microarray and microfluidic devices, are constantly being developed to satisfy the growing demand for sensitive and high-throughput bio-chemical screening platforms, by exploiting in-vitro receptor–ligand interactions. Owing to its recyclability, and robust mechanical and optical properties, poly(methyl methacrylate) (PMMA) has become the most sought after material for the large-scale fabrication of lab-on-a-chip platforms. However, the chemical inertness of PMMA entails the use of complex chemical surface treatments for covalent immobilization of receptor proteins. In addition to being hazardous and incompatible for large-scale operations, conventional bio-functionalization strategies pose high risks of compromising the biomolecular conformations, as well as the stability of PMMA.

In this chapter (**as published in [2]**), we discuss the coupled effect of radio frequency (RF) air plasma and standard 1-ethyl-3-(3-dimethylaminopropyl) carbodiimide (EDC), N-hydroxysuccinimide (NHS) chemistry, to achieve a simple yet scalable PMMA functionalization strategy for covalent immobilization (chemisorption) of proteins. By utilizing green fluorescent protein (GFP) as a model system, we demonstrate that the surface density of chemisorbed proteins is shown to be highly dependent on the air plasma energy, initial protein concentration and the buffer pH. Here, a maximum GFP surface density of 4×10^{-7} moles/m² is obtained, when chemisorbed on EDC–NHS activated PMMA exposed to 27 kJ of air plasma, at pH 7.4.

Furthermore, antibody-binding studies validate the preserved biofunctionality of

the chemisorbed receptor GFP molecules. Finally, the coupled air plasma and EDC–NHS PMMA bio-functionalization strategy is used to fabricate microfluidic antibody assay devices to detect clinically significant concentrations of *Chlamydia trachomatis* specific antibodies. Thus, we elucidate the potential of fabricating sensitive, reproducible and sustainable high-throughput protein screening systems, without the need for harsh chemicals and complex instrumentation.

1.2 Published Article

Shivani Sathish, Noriko Ishizu, and Amy Q. Shen. "Air plasma-enhanced covalent functionalization of poly(methyl methacrylate): high-throughput protein immobilization for miniaturized bioassays." ACS Applied Materials & Interfaces. 11.49 (2019): 46350-46360 [2].

1.3 Conclusions

In this chapter, radio-frequency (RF) air plasma was exploited to covalently tether receptor proteins within poly(methyl methacrylate) (PMMA) microfluidic bioassay devices at high-throughput. We observed that 27 kJ of air plasma generated carboxyl (COOH)-rich PMMA surfaces with the highest affinity towards a wide range of receptor proteins, namely, immunoglobulin G (IgGs), streptavidin and major outer membrane proteins (MOMP) of *Chlamydia trachomatis*, when coupled with 1-ethyl-3-(3-(dimethylamino)propyl) carbodiimide (EDC) and N-hydroxysuccinimide (NHS) chemistry, at a pH of 7.4. These receptor-coated PMMA devices served as effective microfluidic bioassay systems to capture and detect complimentary ligand antibodies.

The rapid and scalable, yet controlled bio-functionalization method serves as a benchmark platform to fabricate reproducible, high-throughput protein screening systems, further driving innovations in chemical and bio-chemical screening assays. In the following chapter, we discuss the integration of the developed MOMP-functionalized PMMA microfluidic antibody chips, with a modular Fluid Handling Device (FHD) to serve as a “proof-of-concept” manually operated point-of-care (POC) device for the detection of anti-MOMP (chlamydia) immunoglobulin G (IgG) antibodies.

Chapter 2

“Proof-of-concept modular fluid handling prototype integrated with microfluidic biochemical assay modules for point-of-care testing” *(Originally published as [1])*

2.1 Introduction

Over the past decades, point-of-care testing kits have been developed to circumvent the reliance on laboratories, by allowing users to perform preliminary health or environmental testing from the privacy of their homes. However, these kits heavily rely on the precision of the user to perform the procedures, leading to increased variability in final assessments.

In this chapter (**as published in [1]**), we present an integrated, completely sealed and disposable point-of-care testing prototype that exploits the benefits of microfluidics and 3D-printing fabrication techniques. The palm-sized modular prototype consists of a manually-operated Fluid Handling Device that allows precise mixing, filtration and delivery of fluids to an on-board microfluidic assay unit (discussed in Chapter 1), for subsequent detection of specific biochemical analytes, with minimized risk of contamination and reduced user-induced errors..

2.2 Published Article

Shivani Sathish, Kazumi Toda-Peters, and Amy Q. Shen. "Proof-of-concept modular fluid handling prototype integrated with microfluidic biochemical assay modules for point-of-care testing." View 1.1 (2020): e1 [1].

2.3 Conclusions

In this chapter, we presented a palm-sized modular Fluid Handling Device (FHD) that allowed precise mixing, filtration, and delivery of fluids to the PMMA microfluidic bioassay devices presented in Chapter 1. These integrated systems enabled the detection of *C. trachomatis* specific antibodies, with a limit of detection (LoD) of 7 nM within 15 mins, serving as a “proof-of-concept” manually operated point-of-care (POC) testing device.

We discussed the development of proof-of-concept microfluidic POC bioassay systems in Chapters 1 & 2. Although we achieved the detection of clinically significant concentrations of antibodies within 15 minutes using the developed devices, issues regarding sample volume requirements and sensitivity of the microfluidic assay modules were observed.

In the following chapters, we delve into the fundamentals of microfluidic biochemical reactions to investigate those parameters that influence the sensitivity, speed and volume requirements of the devices. We diverge from thermoplastic microfluidic systems, and focus on more traditional glass-based microfluidic systems that are easy to integrate with conventional fluorescence microscopes and are able to withstand high flow rates without leakage. Additionally, glass substrates are naturally more hydrophilic than thermoplastic substrates, and can be easily chemically modified to enable covalent protein immobilization. The hydrophilic nature of glass surfaces ensures reduced non-specific adsorption of proteins, thereby increasing specificity of the biochemical reactions. In what follows, we will first describe a simple surface functionalization technique to pattern proteins on glass substrates, followed by a novel glass 3d printing technique that allows us to fabricate robust 3-dimensional microfluidic channels. These glass-based microfluidic systems are used to investigate the dynamics of biochemical reactions, where we propose design rules for the fabrication of rapid and sensitive bioassay microchips.

Chapter 3

“Microcontact printing with aminosilanes: creating biomolecule micro- and nanoarrays for multiplexed microfluidic bioassays” *(Originally published as [4])*

3.1 Introduction

The sensitivity of a microfluidic bioassay system is primarily determined by the bio-functionalities of the patterned receptor biomolecules. Consequently, the primary goal in developing a robust glass-based microfluidic system is to identify techniques that enable efficient biomolecule immobilization whilst preserving their innate functionalities.

In this chapter (as published in [4]), we discuss a two-step aqueous aminosilane patterning approach to create covalently immobilized micro- and nanoarrays of receptor biomolecules within microfluidic devices. By replacing the conventional organic inking solvent with water, and by enforcing short incubation and contact times, we minimize the diffusion of (3-aminopropyl)triethoxysilane (APTES) into the elastomeric poly(dimethylsiloxane) (PDMS) stamp to preserve the pre-defined patterned features. These APTES patterns are subsequently coupled with different receptor molecules within microfluidic bioassay devices to carry out an aptamer-based immunoassay to detect interleukin 6 (IL6) and an antibody-based immunoassay for the detection of human c-reactive protein (hCRP).

3.2 Published Article

Shivani Sathish^{*}, Sébastien G. Ricoult^{*}, Kazumi Toda-Peters, and Amy Q. Shen. "Microcontact printing with aminosilanes: creating biomolecule micro-and nanoarrays for multiplexed microfluidic bioassays." *Analyst* 142.10 (2017): 1772-1781. [4] ^{*}Equal contribution [4].

3.3 Conclusions

In this chapter, we introduced a simple aqueous based microcontact printing (μ CP) method to pattern arrays of (3-aminopropyl)triethoxysilane (APTES) on glass substrates, with feature sizes ranging from a few hundred microns down to 200 nm (for the first time). Next, these substrates were integrated with microfluidic channels, to covalently couple DNA aptamers and antibodies with the micro- and nanopatterned APTES. As these receptors are covalently tethered to the device substrates, the resulting bonds enable them to withstand the high shear stress originated from the flow in these devices. We further demonstrated the multiplexing flexibility of this technique, by immobilizing multiple receptor proteins onto these APTES-patterned substrates using liquid-dispensing robots. Next, to validate the functionalities of these microfluidic bioassay devices, we performed (i) aptamer-based sandwich immunoassays to detect human interleukin 6 (IL6); and (ii) antibody-based sandwich immunoassays to detect human c-reactive protein (hCRP) with a limit of detection of 4 nM, a level below the range required for clinical screening. Lastly, the shelf-life potential of these ready-to-use microfluidic bioassay devices was validated by effectively functionalizing the patterns with receptors up to 3 months post-printing.

In the following chapter, we use this simple patterning technique to immobilize proteins onto fused silica substrates to create truly 3D microfluidic channels. These 3D microfluidic channels are employed to investigate the dynamics of receptor–ligand interactions, to provide design rules to fabricate rapid and sensitive microfluidic bioassay devices.

Chapter 4

Kinetic Enhancement of Receptor–Ligand Interactions in Modular Glass Microfluidic Bioassay Devices (*Unpublished*)

4.1 Introduction

The ability of surface-based biosensors to rapidly detect receptor–ligand binding events at the interface between a liquid and a solid surface, is heavily influenced by three competing transport phenomena, i.e., convection, diffusion and reaction. Depending on the slowest phenomena dominating in the system, the microfluidic devices commonly operate in convection-limited, diffusion-limited, or reaction-limited regimes. In static biosensing systems, the ligand molecules that are in close proximity to the receptor-coated surfaces, i.e., the reaction site, react with the receptors. The ligands diffuse from the preceding layers to replenish the consumed ligands in the later layers as the reaction proceeds. This results in the formation of a steady gradient of ligand concentrations, where the highest ligand concentrations can be seen at a certain distance away from the reaction site. Consequentially, the speed of the biosensor is solely determined by the time taken for the ligand molecules to diffuse across this concentration gradient and reach the receptor-coated surfaces, resulting in *diffusion-limited receptor–ligand binding* [56, 59].

On the contrary, *convection-limited receptor–ligand binding* is commonly observed in nanofluidic systems, where the biomarkers are able to diffuse to the receptor-coated surfaces faster than they are convected through the channels, due to reduced length scales [57]. These *mass transport limitations* contribute to the slow biomarker detection rates in surface-based bioassay systems.

To overcome mass transport-limited receptor–ligand binding, active fluid transport systems such as orbital mixers and microfluidic devices [71, 72] have been integrated with biosensing surfaces in attempt to accelerate the rate of ligand transport to the receptor-coated surface, to be faster than the rate at which ligands react with the receptors. In this scenario, the ligands that are consumed by the reaction site are steadily

replenished by *convection* thereby halting the growth of the ligand concentration gradient. As a result, the speed of the ligand detection is solely determined by the kinetics of the receptor–ligand reactions, resulting in *reaction-limitations* [26, 58, 59].

Currently, most microfluidic systems are being designed to operate in the *reaction-limited regime*, where the ligand solution is continuously flowed (i.e., convected) through the channels to replenish the consumed ligands as they react with the receptor molecules. But, do the previously described analytical solutions still hold for conditions where the ligands are flowed through the channels at extremely fast flow rates?

In this chapter, we aim to answer this question by first creating novel modular 3D glass microfluidic devices that allow us to employ extremely fast flow rates without channel deformations. Using these devices, we monitor the effects of fast flow rates on the real-time binding kinetics between fluorescently-labelled receptor–ligand immunoglobulin G (IgGs) pairs via fluorescence microscopy. We then perform simple numerical simulations to substantiate our experimental observations. With the help of dimensional analysis, we derive dimensionless parameters that allow us to explain our observations by quantifying order-of-magnitude differences between competing phenomena in this system, i.e., *convection*, *diffusion* and *reaction*. Finally, we summarize our observations by providing design rules to support the development of fast and sensitive microfluidic bioassay systems.

4.2 Experimental

4.2.1 Fabrication of two-part modular 3D microfluidic bioassay devices

Computer-aided design (CAD) model

The inter-connectable modular microfluidic system consisting of two components: (1) a solid cone and (2) a hollow 3D microfluidic channel, was designed using Rhinoceros[®] 3D modelling software (USA). The solid cone (height of 3.2 mm) was obtained by slicing a 130 μm gap between an outer concentric cone (top surface diameter of 2.79 mm) and the inner solid region (Figure 4.1(a)). Inversely, the hollow microfluidic region was obtained by slicing the regions inside the microchannel boundaries (Figure 4.1(b)). The microchannel (length of 11.4 mm, with height and width of 400 μm) was designed to consist of a solid obstacle in the center of the channel that created a confinement region of height 20 μm . A hollow conical cavity, whose centerline aligns with that of the obstacle, was designed to connect with the solid cone after fabrication. Each component was sliced into a set of well defined contour (red) and hatch lines (blue) to complete the sliced CAD models (Figure 4.1(c-d)). The contours (20 μm intervals) outlined the boundaries of the component surfaces and the hatches (10 μm intervals) divided the bulk regions of the cone and microchannel into differently-sized polyhedra.

Selective laser induced etching (SLE) in fused silica substrates

The sliced CAD models of the cone and microfluidic channel were rendered in fused silica by selective laser induced etching (SLE) using LightFab 3D printer (GmbH,

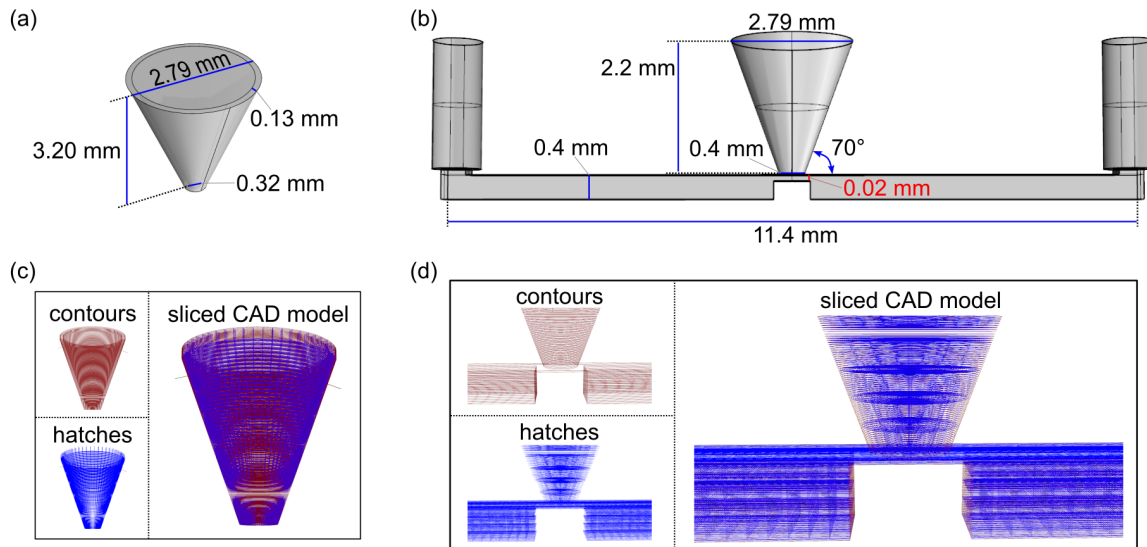


Figure 4.1: Computer-aided design (CAD) model of the modular microfluidic device. Dimensional sketches of the surfaces that outline the boundaries of the (a) cone and (b) microfluidic channel bodies. The sliced CAD models of the (c) cone and (d) confinement region in the microfluidic channel. The sliced model is comprised of contour lines (red), that outline the boundaries, and hatch lines (blue), that section the cone and channel bodies into well-defined polyhedra.

Germany) [17]. The slices served as paths used by the LightFab scanner to modify the fused silica during the printing. Finally the laser-modified regions in the bulk of the fused silica substrate were etched by sonicating in KOH for 72 hours, at 85°C (100 $\mu\text{m/hr}$ etch rate). During this process, the solid cone and hollow channel are obtained by subtractive removal of the etched polyhedrons as designed in the CAD model. The fused silica structures were washed in a sonicated milli-Q water bath at 85°C for 1-2 hrs, to obtain the two components of the modular microfluidic device (Figure 4.2(a-b)).

4.2.2 Immunoglobulin (IgG) bioassay using the assembled 3D modular microfluidic device

The fabricated cones were subsequently sonicated in acetone for 30 mins and patterned on the tips with APTES ((3-aminopropyl)triethoxysilane) by microcontact printing, as previously described in Chapter 3 [4]. The APTES-coated cones (Figure 4.2(a)) were then linked to the receptor biomolecules via 1-Ethyl-3-(3-dimethylaminopropyl) carbodiimide (EDC) and N-Hydroxysuccinimide (NHS) chemistry. For the binding kinetics studies, the cones were incubated in a PBS solution containing 10 $\mu\text{g/ml}$ of AlexaFluor[®] 488 goat anti-mouse immunoglobulins (IgGs) that served as the receptor molecules. The uncoated surfaces of the cones (all regions apart from the cone tip) were coated with black marker ink to prevent light scattering during fluorescence microscopy imaging. The receptor-coated cones were then connected with the conical hollow region of the fabricated 3D microfluidic channel and sealed using Loctite 350 UV cure-adhesive

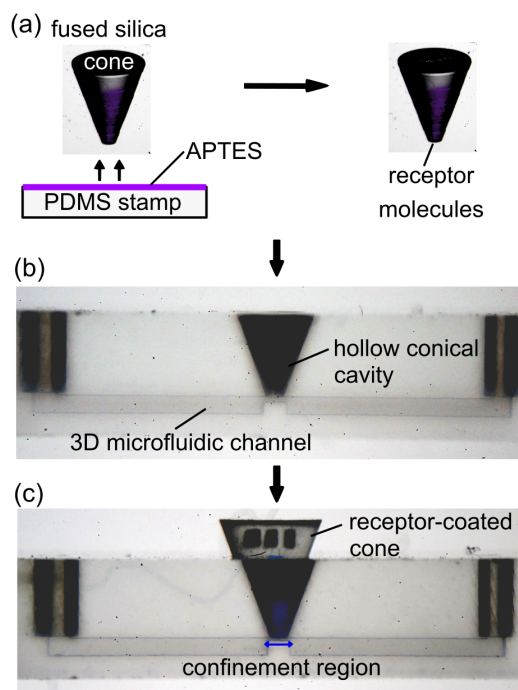


Figure 4.2: Assembly of 3D modular microfluidic bioassay device. (a) Fused silica cones are patterned with APTES by microcontact printing, and then sequentially functionalized with the capture biomolecules with standard EDC–NHS chemistry. (b) The cones are then plugged into the cavity of the 3D microfluidic device and sealed to complete the (c) confinement region in the microfluidic device. The dark markings in the broad regions of the receptor-coated cones are label texts embedded in the cone bulk meant to serve as alignment marks during assembly.

(100% intensity, 10 s exposure) to complete the 3D confinement channels (Figure 4.2(b-c)). The interior surfaces of the microchannels were blocked with 1% bovine albumin solution (BSA) prior to binding kinetic studies to prevent non-specific adsorption of proteins. Varying concentrations (0.125–2 $\mu\text{g}/\text{ml}$) of AlexaFluor[®] 555 rabbit anti-goat IgGs were flushed through the channels at varying flow rates (1–100 $\mu\text{l}/\text{min}$), depending on the binding kinetics study. The median values of all data points were obtained for 3 experimental sets, where the standard deviations are calculated to estimate the experimental uncertainties throughout this study.

4.2.3 Image processing and analysis

The cone tip that served as the reaction site, was imaged from the bottom of the microchannel using the Nikon Ti-E inverted epifluorescence microscope equipped with a CCD camera (Orca Flash v4.0, Hamamatsu photonics). All binding reactions occurring on the cone tip were imaged under a FITC or TRITC filter, at a fixed exposure time of 6 s. For the binding kinetics studies, timelapse images were captured either at a frame rate of 1 image/10 s or 1 image/60 s, for a total capture time of 40 mins. The unprocessed images captured for each dataset were analyzed and processed using MATLAB[®] (Mathworks, Japan) and ImageJ (NIH, USA). The roughness (≈ 30 nm

RMS) inside the microchannel cavity as a result of the SLE process, resulted in heavy light scattering when imaged under the FITC excitation-emission spectral regime. To avoid this issue, IgG receptor-ligand pairs were accordingly chosen to be compatible for imaging in the TRITC excitation-emission spectral regime. Nevertheless, an image of the PBS-filled microchannel was captured prior to flowing fluorescent IgG solutions, to extract the intrinsic background fluorescence intensity for each experimental setup. This background fluorescence intensity was subtracted from all subsequent fluorescent images captured during the binding kinetics study. Following background subtraction, the median pixel intensity per μm^2 area for the selected regions of interest (ROI) was extracted for each image and used for subsequent analyses. All data have been graphically depicted using OriginPro2017 (OriginLab, USA). Additionally, the images were processed post quantification to increase the contrast through linear modifications in ImageJ for visual depiction.

4.3 Theory

4.3.1 Defining the region of interest in the microfluidic system

The 3D microfluidic device used in this study (Figure 4.2 & illustrations in Figure 4.3) is composed of a single straight channel of width W , height H and a rectangular obstacle (length l , width w) located in the center of the channel that creates a confinement region of height h . This confinement region, is considered as the region of interest in this study, where $w = W$. A circular reaction site with diameter d , whose center is aligned with the center of the obstacle, is located on the top wall of the microchannel, at a height h above the obstacle. The reaction site spans the entire width of the confinement region. This reaction site is composed of receptors (blue spheres in Figure 4.3) that serve to capture the target ligands. The target biomarker solution consisting of ligands (red sticks in Figure 4.3) is flowed through the channel with an initial concentration of C_0 , at a constant pressure-driven flow rate, Q . The dimensions of the fabricated microchannels and flow rates used in this study are listed in Table 4.1.

In the region of interest, i.e., the confinement region (Figure 4.4), the width of the obstacle is sufficiently larger than the confinement height ($w=8.2h$). Hence, the flow in these channels is assumed to be unidirectional and invariant along the width of the channel (i.e., along the z -axis). As a result, the transport phenomena in these channels can be approximated to be 2-dimensional (2D), where the boundary effects from the side walls of the channel are neglected. In addition, the fluid is assumed to be incompressible and Newtonian. The flow is assumed to be axial and steady. The effects of gravity are neglected due to the relatively small height of the confinement, and the

Table 4.1: Dimensions and flow rates used in the 3D microchannel, shown in Figure 4.3

W & w (μm)	H (μm)	h (μm)	l (μm)	d (μm)	Q ($\mu\text{l}/\text{min}$)
447.2 \pm 2.3	455.0 \pm 3.1	54.7 \pm 3.6	534.6 \pm 1.4	399.0 \pm 11.3	0 – 100

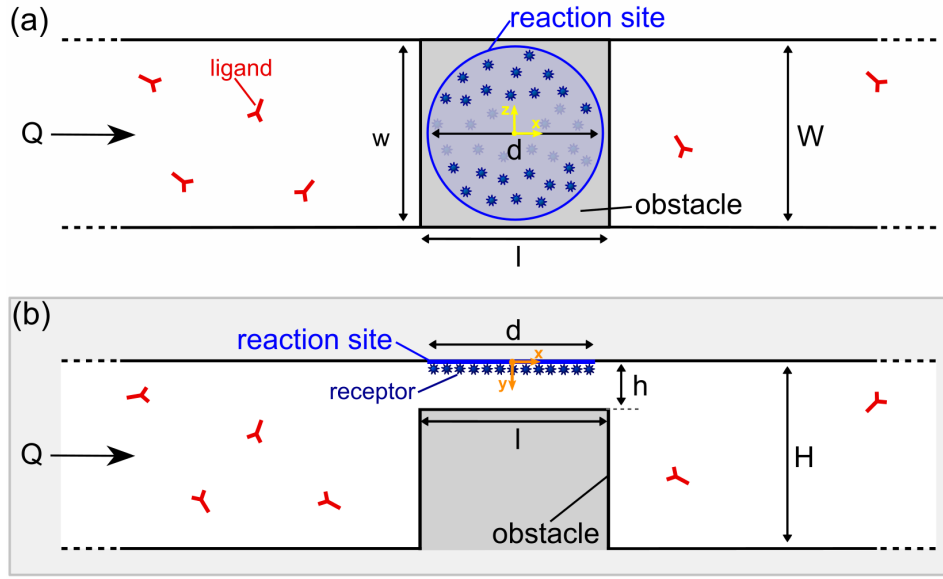


Figure 4.3: Schematic of the microchannel cross section. (a) Bottom view and (b) side view of the microchannel of width W , height H , confinement width w , length l and height h , and reaction site diameter d . The reaction site, at a height h directly above the obstacle (top channel wall), consists of immobilized receptors (blue spheres). These molecules capture specific ligands (red sticks) flushed through the channel with a flow rate Q . The origin of the coordinate system is placed at the center of the reaction site, on the top wall of the microfluidic channel.

changes in physical properties of the fluids due to temperature fluctuations are assumed to be insignificant. The micrometer-scale dimensions of the microfluidic system ensure that the flow within the channels is laminar. The 2D channel geometry is described by the Cartesian coordinate system, where the origin of the coordinate system is at the center of the reaction site. A 1-dimensional (1D) immunoreaction (along x-axis, i.e., the axial direction) occurs on the reaction site (region 4 in Figure 4.4) between the receptors and ligands. This criterion is only valid when the ligand concentration is assumed to be constant along the width of the confinement region.

4.3.2 Estimating the flow field in the confinement region

In accordance with the above assumptions, the flow profile of the buffer solution in the microchannel can be described by the Hagen-Poiseuille law [73], where the fluid (i.e., the ligand buffer solution) velocity can be described by the Navier-Stokes equation. Assuming the flow is steady, the equations are,

$$\rho(\vec{U} \cdot \nabla)\vec{U} = -\nabla p + \mu\nabla^2\vec{U}, \quad (4.1)$$

$$\rho(\nabla \cdot \vec{U}) = 0, \quad (4.2)$$

where $\vec{U}(x,y)=u(x,y)\hat{e}_x+v(x,y)\hat{e}_y$ is the 2D fluid velocity, p is the pressure within the flow field, and ρ and μ are the buffer solution's density and dynamic viscosity

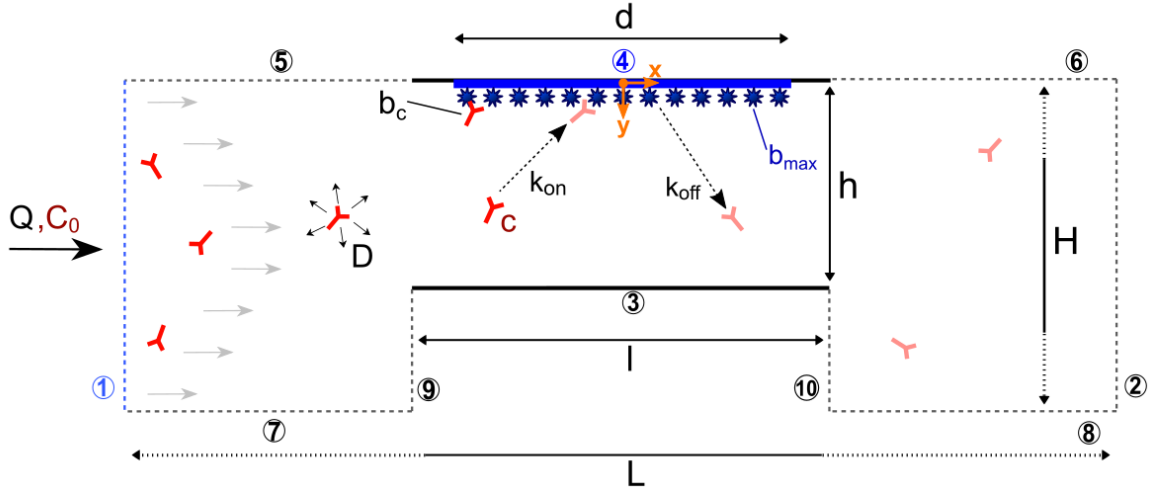


Figure 4.4: Schematic of the confinement region with labelled boundaries. The region of interest, i.e., the confinement region (solid lines) of length l and height h , consists of the reaction site (diameter d) immobilized with receptors (blue spheres) with a surface concentration of b_{max} . The ligands (red sticks) are flowed in solution through the channel at a flow rate Q , and an initial concentration of C_0 , with a diffusion coefficient of D . The concentration of ligands close to the reaction site is c . The ligands react with the immobilized receptors with an association and dissociation constant k_{on} and k_{off} respectively, to form the receptor–ligand complex, where the surface concentration of the complex is b_c . Dotted lines illustrate the extended regions of the microfluidic channel outside the confinement region (height, H and length, L). The boundaries of the system are numbered from 1-10. The origin of the coordinate system is placed at the center of the reaction site, on the top wall of the microfluidic channel.

respectively. As illustrated in Figure 4.3, $w \gg h$ in the confinement region, which entails $\vec{u}(x,y) \gg \vec{v}(x,y)$. Additionally, assuming the flow is unidirectional, $\vec{u}(x,y)$ can be simplified to $\vec{u}(y)$ along the axial direction. The parabolic velocity profile can thus be described as,

$$\vec{u}(y) = u(y)\hat{e}_x = \frac{1}{2\mu} \frac{\partial p}{\partial x} y(y-h)\hat{e}_x, \quad (4.3)$$

where $\partial p/\partial x$ is the negative axial pressure gradient and \hat{e}_x is the unit normal vector in the x-direction. Next, the average velocity in the confinement region u_{avg} , is calculated by integrating the velocity field over the confinement height. Therefore, the volumetric flow rate Q , defined as the product of u_{avg} and cross-sectional area ($h \times w$) is

$$Q = w \int_0^h u(y)dy = -\frac{wh^3}{12\mu} \frac{\partial p}{\partial x}. \quad (4.4)$$

This equation is substituted into equation 4.3 to obtain the expression for the

parabolic velocity field in the microchannel:

$$\vec{u}(y) = \frac{6Q}{h^3w}y(h-y)\hat{e}_x. \quad (4.5)$$

4.3.3 Mass transport

The spatio-temporal evolution of the ligand concentration field $c(x, y, t)$ in the confinement region is governed by the additive effect of molecular diffusion and convection due to flow, that can be described by the convection–diffusion equation:

$$\frac{\partial c}{\partial t} = D\nabla^2 c - \vec{U} \cdot \vec{\nabla} c, \quad (4.6)$$

where $c(x, y, t)$ is the ligand concentration field, and D is the diffusion coefficient of the ligands in the buffer fluid. The boundary conditions for the ligand concentration field are defined as:

$$c = C_0 \quad \text{at surface (1) in Figure 4.4,} \quad (4.7)$$

$$\vec{n} \cdot D\nabla c = 0 \quad \text{at surfaces (3) and (5)-(10) in Figure 4.4,} \quad (4.8)$$

where \vec{n} is defined as the unit normal vector directed out of the surface. Boundary condition 4.7 ensures that the solution introduced into the channel has an initial ligand concentration of C_0 at the inlet, while boundary condition 4.8 imposes that no ligands diffuse out of the channel walls.

4.3.4 Receptor–ligand reaction kinetics

When in close proximity, the ligand molecules reversibly bind to the receptor molecules at the liquid–solid interface at the reaction site. Several reaction models have been proposed to describe the receptor–ligand binding mechanisms [74, 75]. In this study, we assume that the receptor–ligand binding reaction occurring on a solid surface is analogous to the reaction between adsorbates in a fluid and adsorbents on a solid surface. Given this assumption, the receptor–ligand binding mechanism can be described by the Langmuir adsorption isotherm model [76]. This model has been described to effectively generalize majority of the adsorption/desorption mechanisms in molecular biology [58]. Specifically, the Langmuir model describes the pseudo-first order binding reaction between the ligand in solution, and the receptor immobilized on the reaction site surface, given that (1) the ligand molecules reversibly bind to a finite number of receptor molecules on the reaction site, (2) one receptor molecule binds to one ligand molecule equivalently for all binding sites under isothermal conditions, and (3) the receptor–ligand binding saturates at equilibrium. Specifically,



where k_{on} and k_{off} are the association and dissociation constants respectively. The

temporal evolution of the *complex* concentration (b_c) can be estimated as,

$$\frac{\partial b_c}{\partial t} = k_{on}c(b_{max} - b_c) - k_{off}b_c, \quad (4.10)$$

where, c is the concentration of *ligands* close to the reaction site, b_{max} is the surface concentration of *receptors* on the reaction site and b_c is the surface concentration of *receptors*, bound to *ligand* molecules. Here, the temporal evolution of b_c ($\partial b_c/\partial t$) is monitored to quantify the rate of formation of the *receptor–ligand complex*.

Correspondingly, the reaction–flux balance boundary condition is imposed on surface (4) in Figure 4.4,

$$\frac{\partial b_c}{\partial t} = -D \frac{\partial c}{\partial y} \quad \text{at surface (4)}. \quad (4.11)$$

Equation 4.11 defines the boundary condition that describes the balance between the diffusive flux of ligands perpendicular to the reaction site, and the binding rate of the receptor–ligand reactions.

Table 4.2: Operational parameters employed in this study

Parameter	Units	Quantity	Reference
ρ	kg/m ³	9.98×10^2	[77]
μ	kg/m.s	1.0×10^{-3}	[78]
D	m ² /s	44.0×10^{-12}	[79]
b_{max}	moles/m ²	1.0×10^{-9}	[57]

4.3.5 Scaling analyses

The governing equations listed in Sections 4.3.3 & 4.3.4 are non-dimensionalized to derive approximate scaling solutions and dimensionless parameters. These scaling solutions pave ways to perform comparative analyses of interdependent flow and reaction parameters employed in this system.

Non-dimensionalized mass transport equation

Equation 4.6 is non-dimensionalized by scaling the ligand concentration by the initial ligand concentration C_0 , the axial distance scaled by the diameter of reaction site (d), transverse distances by the confinement height (h), and time by the characteristic time (equation 4.12). At low flow rates, only those ligands that diffuse across the height of the confinement towards the reaction site, are able to bind to the immobilized receptors. Hence, the characteristic time that emulates this phenomenon, is the time (t_D) taken for the ligands to diffuse across the confinement height to reach the reaction site:

$$c^* = \frac{c}{C_0}, \quad x^* = \frac{x}{d}, \quad y^* = \frac{y}{h}, \quad t^* = \frac{t}{t_D} = \frac{Dt}{h^2}. \quad (4.12)$$

Thus, the non-dimensionalized expression of equation 4.6 (indicated by stars) is:

$$\frac{\partial c^*}{\partial t^*} = \beta^2 \frac{\partial^2 c^*}{\partial x^{*2}} + \frac{\partial^2 c^*}{\partial y^{*2}} - (6\beta Pe_h) y^* (1 - y^*) \frac{\partial c^*}{\partial x^*}, \quad (4.13)$$

where, $Pe_h = Q/wD$ is the bulk Peclet number, which is the ratio of convective to diffusive ligand transport within the confinement region, and $\beta = h/d$ is the aspect ratio of the confinement height to the diameter of the reaction site. As the supplied ligands are steadily captured by the receptors at the reaction site, a steady depletion zone with thickness δ is formed.

While Pe_h describes the dominance of diffusion (when, $Pe_h \ll 1$) versus convection (when, $Pe_h \gg 1$) of antibodies in the confinement zone at low flow rates, it does not encapsulate the effect of linear shear flow, when extremely fast flow rates are employed in the system.

At extremely fast flow rates, the ligands are flushed downstream before they have a chance to diffuse across the confinement height, h . In this case, the reaction site does not experience the effect of the full parabolic flow profile, but is most affected by the linear flow profile (equation 4.14) up to a certain height close to its surface,

$$u = \dot{\gamma}_{(y=0)} \times y, \quad (4.14)$$

$$\dot{\gamma}_{(y=0)} = \frac{6Q}{wh^2}, \quad (4.15)$$

where, $\dot{\gamma}_{(y=0)}$ is the shear rate at the reaction site ($y = 0$). In the case of high local velocities, the diffusive ligand flux is independent of confinement height, but dependent on the steady depletion zone thickness, δ . At this distance close to the reaction site, those ligands that are convected by the linear flow across the length (d) of the reaction site ($t_c = d/\dot{\gamma}_{(y=0)}\delta$), have just enough time to diffuse across δ to reach the reaction site ($t_\delta = \delta^2/D$). This results in a new characteristic time scale (t_δ) that describes the time taken for an ligand to diffuse across the depletion zone, with thickness $\delta = (dD/\dot{\gamma}_{(y=0)})^{1/3}$, at high flow rates.

By accounting for these new spatial and temporal scales arising at enhanced local flow conditions, the convection-diffusion equation (equation 4.6) can be scaled with the following parameters, as described below:

$$c^* = \frac{c}{C_0}, \quad x^* = \frac{x}{d}, \quad y^* = \frac{y}{\delta}, \quad t^* = \frac{t}{t_\delta} = \frac{Dt}{\delta^2}. \quad (4.16)$$

Thus, the new non-dimensionalized expression of equation 4.6, that incorporates the effect of linear flow in the boundary layer, is

$$\frac{\partial c^*}{\partial t^*} = \left(\frac{1}{Pe_\delta} \right)^{2/3} \frac{\partial^2 c^*}{\partial x^{*2}} + \frac{\partial^2 c^*}{\partial y^{*2}} - y^* \frac{\partial c^*}{\partial x^*}, \quad (4.17)$$

where,

$$Pe_\delta = \frac{\dot{\gamma}_{(y=0)} d^2}{D} = \frac{6Pe_h}{\beta^2}. \quad (4.18)$$

Equation 4.18 defines the local Peclet number (Pe_δ) in the confinement region, relating the bulk Peclet number (Pe_h) and the aspect ratio of the confinement region (β). Pe_δ enables us to quantify the competition between diffusive transport of the ligands and transport of ligands by linear convective flow, in the vicinity of the reaction site.

Additionally, the boundary conditions 4.7 & 4.8 are non-dimensionalized using the same scaling analyses as described above to obtain:

$$c^* = 1 \quad \text{at surface (1),} \quad (4.19)$$

$$\vec{n} \cdot \left[\left(\frac{1}{Pe_\delta} \right)^{1/3} \left(\frac{\partial c^*}{\partial x^*} \hat{e}_x \right) + \left(\frac{\partial c^*}{\partial y^*} \hat{e}_y \right) \right] = 0 \quad \text{at surfaces (3) and (5)-(10).} \quad (4.20)$$

Non-dimensionalized receptor–ligand reaction kinetic equation

The governing equation for receptor–ligand reaction kinetics (equation 4.10) can be non-dimensionalized to derive a dimensionless parameter that describes the balance between the transport and reaction time scales. Here, the concentration of bound *receptors* (b_c) is scaled by the surface concentration of immobilized *receptors* (b_{max}), c is scaled by the initial *ligand* concentration C_0 , and time is scaled by the time taken for the ligands to diffuse across the depletion layer height ($t_\delta = \delta^2/D$):

$$b^* = \frac{b_c}{b_{max}}, \quad c^* = \frac{c}{C_0}, \quad t^* = \frac{Dt}{\delta^2}. \quad (4.21)$$

Consequently, the non-dimensionalized expression of equation 4.10 becomes

$$\frac{\partial b^*}{\partial t^*} = \frac{C_0 k_{on} \delta^2}{D} c^* (1 - b^*) - \frac{\delta^2 k_{off}}{D} b^*, \quad (4.22)$$

which can be further simplified to yield

$$R = \frac{\partial b^*}{\partial t^*} = Da_{diffusion} c^* (1 - b^*) - Da_{off} b^*, \quad (4.23)$$

where $Da_{diffusion} = C_0 k_{on} \delta^2 / D$ and $Da_{off} = \delta^2 k_{off} / D$ are the Damkohler numbers that represents the ratio of the reactive flux to the diffusive flux for the association and dissociation reactions respectively.

Correspondingly, the boundary condition 4.11 is non-dimensionalized using the same scaling analyses as described above to obtain:

$$\frac{\partial b_c^*}{\partial t^*} = -\phi \frac{\partial c^*}{\partial y^*} \quad \text{at surface (4),} \quad (4.24)$$

where, $Pe_\delta = \dot{\gamma}_{(y=0)} \delta^2 / D$ in equation 4.18, and, $\phi = C_0 \delta / b_{max}$. Furthermore, with reference to equation 4.34, equation 4.24 can be rewritten as:

$$\frac{\partial c^*}{\partial y^*} = -\frac{1}{\phi} \left[Da_{diffusion} c^* (1 - b^*) - Da_{off} b^* \right]. \quad (4.25)$$

Here, equation 4.25 is the dimensionless reaction–flux balance boundary condition, where the dimensionless quantity ϕ is termed as the “*binding fraction*”. This dimensionless quantity can be used to ensure that the surface concentration of immobilized *antigens* (b_{max}) is always higher than $C_0\delta$.

4.4 Numerical Simulation

The evolution of the depletion zone (thickness of δ) with sequentially increasing Pe_δ in the confinement region was modelled using the finite element COMSOL Multiphysics[®] software (COMSOL, Sweden) algorithms. The device geometry and domains were defined according to Figure 4.4 using the dimensions listed in Table 4.1. The computational mesh consists of 166826 free triangular domain elements with minimum and maximum element sizes of $0.0682 \mu\text{m}$ & $5.91 \mu\text{m}$, with a maximum element growth rate of $1.08 \mu\text{m}$. In addition to the free triangular domains, the boundaries of the device geometry were emphasized using the boundary layer mesh, with a boundary layer stretching factor of 1.05 for a total of 9 layers, where the thickness of the first layer was defined to be $0.5 \mu\text{m}$. The edges of the geometry were refined with the in-built corner refinement algorithm, where the minimum angle between boundaries was set to be 240° , with an element size scaling factor of 0.25. The mesh quality was inspected until data convergence was observed using the optimized mesh. Figure 4.5 demonstrates that the final mesh consists of optimal elements within the device geometry (green domains indicate the best quality of 1).

The microchannel boundaries were divided into 10 surfaces as illustrated in Figure 4.4, where the reaction site was defined by surface 4. The bulk laminar flow field

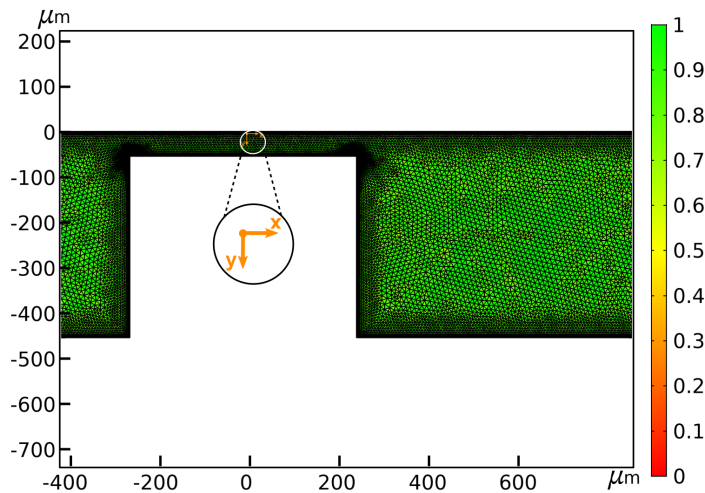


Figure 4.5: Image demonstrating the mesh quality of the COMSOL model. The computational mesh for the defined device geometry was constructed with a mixture of free triangular domains and boundary layers. The geometry edges were refined using the corner refinement algorithm, until a quality of 1 (green domains) was obtained. The mesh quality of 1 indicates the presence of optimal elements in the mesh domain.

and transport of diluted ligand species at steady state were modelled by solving the dimensional Navier-Stokes equations (equations 4.1 & 4.2) coupled with the dimensional convection-diffusion equation (equations 4.6). The assumptions listed in Section 4.3.1 were imposed for all the simulations. The boundary and initial conditions were imposed based on equations 4.7 & 4.8. An initial ligand concentration (C_0) of 6.67 mol/m^3 was used for all the simulations, to be consistent with the experimental C_0 employed in this study. The receptor–ligand binding reaction was modelled on surface 4, using the dimensional Langmuir adsorption model (equation 4.9 and boundary condition 4.11). As the dissociation constant $k_{off} < 10^{-5} \text{ s}^{-1}$ has been reported for moderate affinity IgG–IgG binding reactions [80, 81], the “rapid irreversible surface reactions” module (i.e., $k_{off} = 0$) was chosen as a limiting case for the COMSOL simulations. The solutions of the velocity and concentration fields were obtained using the Generalized Minimal Residual iterative solver and the in-built PARDISO course solver. The raw data from the simulations were extracted and graphically represented using Origin-Pro2017 (OriginLab, USA).

4.5 Results and discussion

4.5.1 Defining local Peclet number (Pe_δ) to characterize ligand transport in the 3D microfluidic channels

Microfluidic systems have been employed to actively transport ligands to the receptor-coated reaction surfaces, in an attempt to overcome mass transport limitations and achieve kinetic enhancement of receptor–ligand interactions at liquid–solid interfaces. In this section, we use scaling analysis to characterize the ligand transport within the fabricated 3D microfluidic channels. Furthermore, we describe the mechanisms that drive the targeted delivery of ligand molecules to the reaction site, placed in parallel to the flow direction.

In this study, the 3D modular microfluidic device is composed of two interlocking components: (1) a solid fused silica cone (Figure 4.2a), whose tip is coated with receptor molecules that are covalently linked to APTES patterned on the tip surface via a previously described microcontact printing method [4], and (2) a straight 3D microchannel embedded in fused silica, composed of a rectangular obstacle positioned at the center of the channel. The region above the obstacle is hollowed out conically to allow subsequent locking with the complimentary fused silica cone (Figure 4.2b-c), to create a confinement region of height h above the obstacle (Figure 4.6a). This confinement region encapsulating the receptor-coated cone tip that serves as the reaction-site, is defined as the region of interest in this study.

A ligand solution consisting of fluorescently-labelled immunoglobulins (IgGs) (red sticks in Figure 4.6a), suspended in PBS (phosphate buffered saline), is flowed through the microchannel at varying flow rates, Q (table 4.1). The reaction site is coated with complimentary fluorescent IgGs (blue spheres in Figure 4.6a) that serve as receptors to capture the ligand IgGs. The details of the IgG pair have been listed in Section 4.2.2. In accordance with the assumptions listed in Sections 4.3.1 & 4.3.2, the flow conditions that enabled the ligand IgG solution to attain fully developed laminar flow profiles

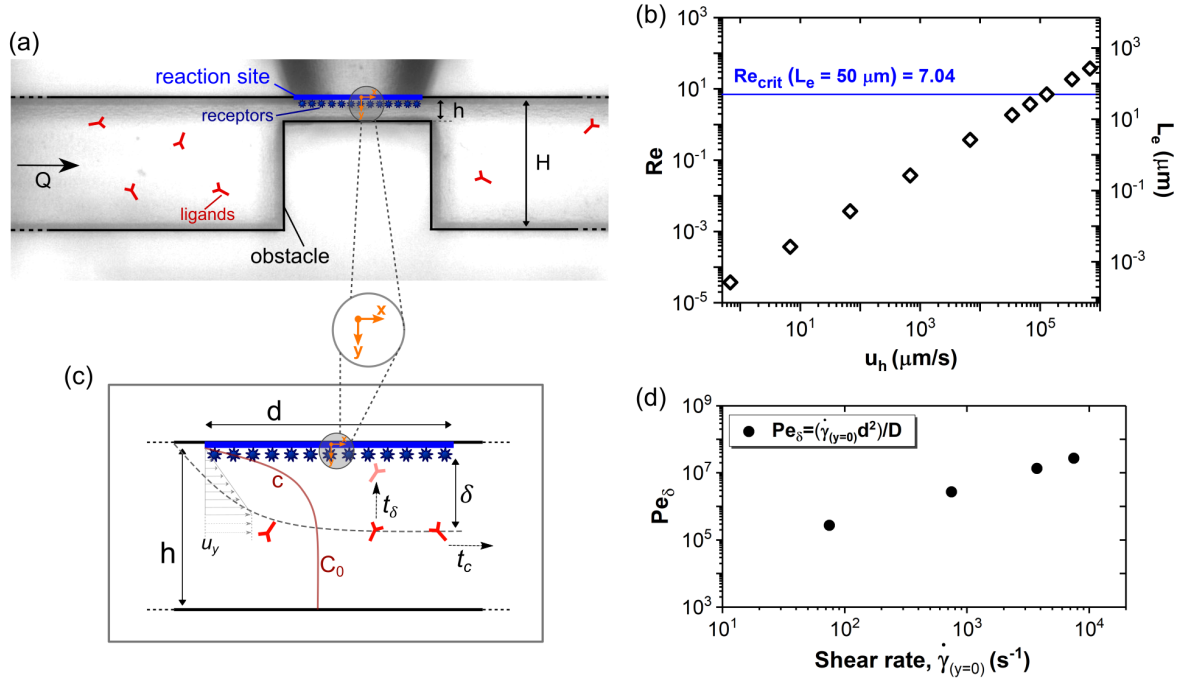


Figure 4.6: Ligand transport through the 3D microfluidic channel. (a) Descriptive stereomicroscopic cross-section image of the assembled 3D modular microfluidic bioassay device, with channel height H and confinement height h . Ligands (red sticks) are flowed through the microchannel with a flow rate Q and react with the receptors (blue spheres) patterned on the reaction site. (b) Reynolds number (Re) and entrance length (L_e) plotted as a function of axial flow velocity (u_h). (c) Schematic illustrating the steady ligand depletion layer formed in the confinement region of the device. (d) Local Peclet number ($Pe_\delta = \dot{\gamma}_{(y=0)} d^2 / D$) plotted against the shear rates ($\dot{\gamma}_{(y=0)}$) experimentally investigated in this study.

in the vicinity of the reaction site were identified and employed for this study. As seen in Figure 4.6b, the Reynolds numbers (Re , characterized as $Re = \rho u_h h / \mu$) were observed to be below the critical Reynolds number (Re_{crit}), where, Re_{crit} is defined as the Re at which the entrance length ($L_e = 0.13 Re$) is equal to the distance between the starting points of the obstacle and the reaction site (measured to be $50 \mu\text{m}$). $Re < Re_{crit}$ is indicative of fully developed laminar flow [82] for flow velocities between $10^{-1} < u_h < 10^5 \mu\text{m/s}$. Due to the potential complications arising from transient flow effects on the receptor–ligand kinetics, faster flow velocities ($u_h > 10^5 \mu\text{m/s}$), were not employed in this study as the flow profile is not fully developed near the reaction site when $Re > Re_{crit}$.

At extremely low Re ($Re < 10^{-4}$), purely diffusive transport of ligand IgGs to the reaction site is observed, as described by the low Peclet numbers ($Pe_h \ll 1$). Here, $Pe_h = Q/wD$ is defined as the ratio of convective to diffusive ligand transport, obtained from the non-dimensionalized convection–diffusion equation (equation 4.13), described in Section 4.3.5. Diffusion-driven ligand transport at $Pe_h \ll 1$ is not considered in this study. Instead, we focus our investigations on purely convection dominant ligand transport. In particular, we experimentally investigate the receptor–ligand kinetics at

$Pe_h \gg 10^2$, achieved at $Re > 10^{-1}$.

As the ligand IgGs are convected through the confinement region, those molecules close to the reaction site are gradually consumed as a result of the binding reaction with the receptor IgGs. As a consequence, the ligand IgG concentration close to the reaction site (c) is much lower than the bulk ligand IgG concentration (C_0), creating a steady ligand concentration boundary layer above the reaction site. In this study, the boundary layer is termed as the depletion zone, whose thickness is defined as δ . The schematic in Figure 4.6c illustrates the depletion zone created above the reaction site. At $Pe_h \gg 10^2$, the ligand IgGs above δ are swept away without ever interacting with the reaction site. As a result, the ligand convection in the bulk of the confinement region is no longer a dominating factor in this system. On the contrary, the local convection in the vicinity of the reaction site plays a significant role in the transport of ligands to the surface.

While the bulk Pe_h fails to account for the effect of local effects, the dimensionless local Peclet number, $Pe_\delta = \dot{\gamma}_{(y=0)}d^2/D$, allows us to quantify the dominance of local convective flow versus diffusion, in the transport of ligand IgGs to the reaction site (derived in Section 4.3.5). As depicted in Figure 4.6d, convection dominated ligand transport is observed with increasing shear rate $\dot{\gamma}_{(y=0)}$, where $10^3 < Pe_\delta < 10^8$. The effect of enhanced convection-driven ligand transport on the receptor–ligand reaction kinetics will be experimentally investigated for $10^5 < Pe_\delta < 10^8$ in the following sections.

4.5.2 Homogeneous binding of ligands across reaction site at high Pe_δ

While enhanced receptor–ligand binding kinetics is an anticipated outcome of enhanced convective flows, we observed an interesting influence of Pe_δ on the homogeneity of ligand binding across the reaction site. To investigate this effect, we divided the centerline of the reaction site into 7 sequential regions, as illustrated by 7 different symbols in Figure 4.7a. The temporal evolution of ligand IgG binding (for $C_0 = 6.67 \text{ mol/m}^3$) on the reaction site was monitored at these 7 regions of interest (ROIs) individually, starting from time, $t = 0 \text{ min}$, up to $t = 40 \text{ min}$ (red fluorescent images in Figure 4.7a).

The binding kinetics at the reaction site was investigated using the analytical solution of the Langmuir adsorption isotherm (equation 4.10). This analytical solution is obtained under the assumption that the binding reaction is the rate-limiting process at high Pe_δ flows employed in these sets of experiments (where, $10^5 < Pe_\delta < 10^8$). Under this assumption, the ligand IgG concentration (c) close to the reaction site approaches the bulk ligand IgG concentration (C_0). Subsequently, equation 4.10 is analytically solved to obtain

$$b_c(t) = \left(\frac{k_{on}C_0b_{max}}{k_{on}C_0 + k_{off}} \right) (1 - e^{-(k_{on}C_0 + k_{off})t}). \quad (4.26)$$

Equation 4.26 is re-written as

$$f_B = \frac{b_c(t)}{b_{max}} = \left(\frac{C_0}{C_0 + K_D} \right) (1 - e^{-(t/\tau_R)}), \quad (4.27)$$

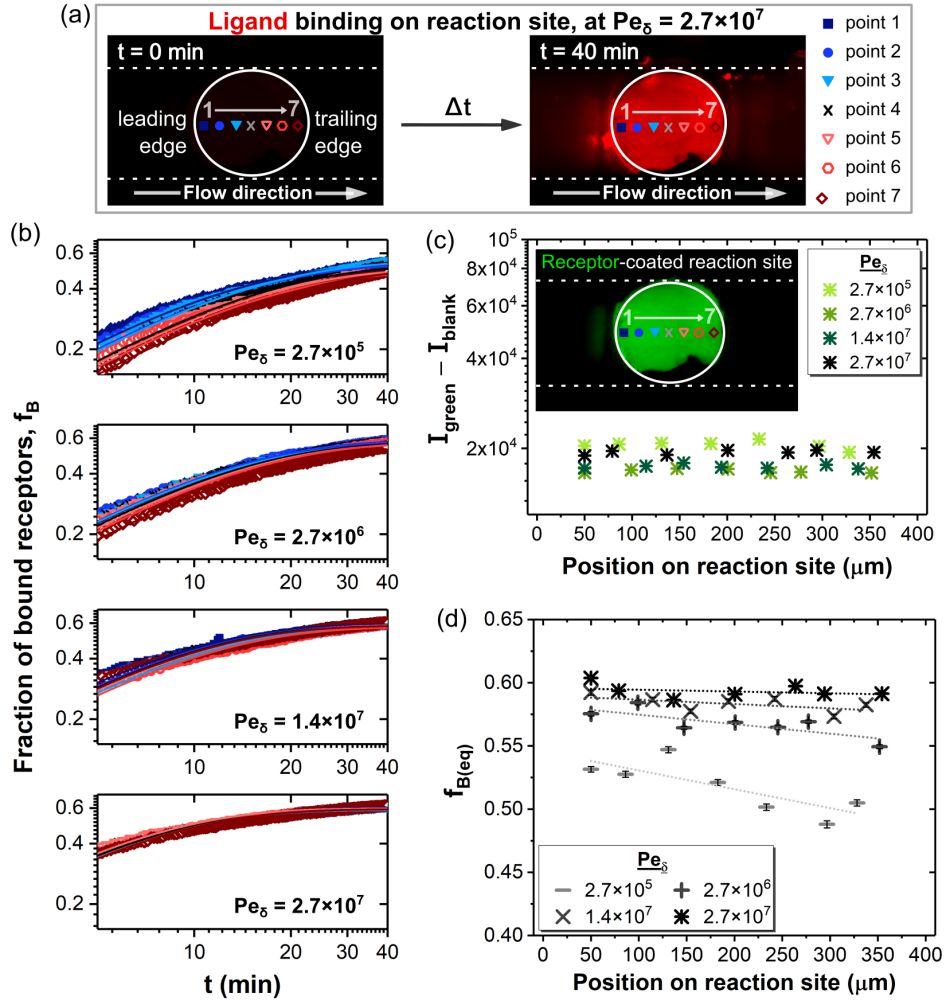


Figure 4.7: Influence of Pe_δ on homogeneity of ligand ligand across reaction site. (a) The fluorescence micrographs show the reaction site before and after capture of ligand IgGs (red), at $t = 0 \text{ min}$ and $t = 40 \text{ min}$, respectively. White circles outline the reaction sites and dotted lines mark the channel boundaries. Symbols marked on the images indicate the 7 regions of interest (ROI) distributed across the centerline of the reaction site, employed in the following graphs. (b) Each graph depicts the evolution of f_B (fraction of bound receptors) as a function of time for the 7 defined ROIs, for experimentally increasing Pe_δ . Each profile is fitted with equation 4.29 to extract the fraction of bound receptors at equilibrium, $f_{B(\text{eq})}$. (c) Normalized fluorescence intensities of immobilized receptors, extracted from the 7 ROIs, plotted as a function of position on reaction site, for varied Pe_δ . Inset fluorescence micrograph depicts the surface of reaction site coated with receptor IgGs (green). (d) $f_{B(\text{eq})}$ plotted as a function of position on reaction site for varied Pe_δ . Dotted lines are apparent linear fits meant to serve as trendlines, and error bars are within the symbols for all displayed data ($n = 3$).

where, $b_c(t)$ is the number of *receptor IgGs* bound with *ligand IgGs* at a given time (t), $K_D = k_{off}/k_{on}$ is the equilibrium dissociation constant and $\tau_R = (k_{on}C_0 + k_{off})^{-1}$ is the time taken for the reaction to equilibrate. Here, f_B is the fraction of bound receptor IgGs. f_B is experimentally measured by calculating the median fluorescence ratios and standard deviations ($n = 3$) of captured ligand IgGs (red) and receptor IgGs (green) from the respective fluorescence micrographs (Figure 4.7a).

Additionally, the fraction of receptor IgGs bound with ligand IgGs at equilibrium (i.e., $\tau_R \rightarrow \infty$) can be estimated as

$$f_{B(eq)} = \frac{b_{eq}}{b_{max}} = \frac{C_0}{C_0 + K_D}. \quad (4.28)$$

The final equation describing the temporal evolution of f_B can be re-written as:

$$f_B = f_{B(eq)}(1 - e^{-(t/\tau_R)}). \quad (4.29)$$

Equation 4.29 is used to fit the experimental data to track the evolution of f_B at the 7 defined ROIs, plotted in Figure 4.7b for increasing Pe_δ . At $Pe_\delta = 2.7 \times 10^5$, the leading edge of the reaction site (i.e., point 1 in Figure 4.7a) was seen to equilibrate faster than the trailing edge (i.e., point 7 in Figure 4.7a). In addition, the varied saturation profiles for the 7 ROIs indicate that the concentration of captured ligand IgGs at equilibrium, is largest at the leading edge (indicated by the saturation of f_B at 0.54), and decreases towards the trailing edge. This decreasing tendency in both saturation speed and captured ligand IgG concentration with increasing distance from the reaction site-leading edge was observed to diminish with increasing Pe_δ .

To eliminate the contribution of inhomogeneities arising from the receptor IgG immobilization, the normalized median fluorescence intensities extracted from the 7 ROIs were plotted against the position on the reaction site for each tested experimental condition ($10^5 < Pe_\delta < 10^8$). As seen in Figure 4.7c, the normalized fluorescence intensity is invariant across all positions on the reaction site centerline, for all of the tested experimental conditions. Additionally, the error bars are within the symbols for all data points, thereby demonstrating minimal experimental variation in fluorescence intensities across different data sets ($n = 3$). This proves that the apparent inhomogeneity in ligand binding observed at low Pe_δ is not a result of inhomogeneous distribution of receptors on the reaction site.

To analytically quantify the concentration of captured ligand IgGs at equilibrium, we extracted the fraction of bound receptor IgGs at equilibrium, $f_{B(eq)}$ from each fitted curve for the respective ROI from the plots in Figure 4.7b. As observed in Figure 4.7d, $f_{B(eq)}$ linearly decreases with distance from the leading edge of the reaction site at $Pe_\delta = 2.7 \times 10^5$. With increasing Pe_δ , $f_{B(eq)}$ becomes more uniform across the reaction site, indicating that the homogeneity of ligand binding across the reaction site is influenced by the inhomogeneity of ligand IgG transport to the reaction site at low Pe_δ . These results indicate that binding uniformity can be achieved by increasing the local Peclet number, i.e., by increasing the flow rates (Q) and/or decreasing the size of the reaction site (d).

4.5.3 Uniform ligand flux across reaction site at high Pe_δ

At extremely high flow rates, the ligand IgGs that diffuse to the receptors across the depletion zone (at time t_δ), are replenished by the carrier fluid flowed through the confinement region (at time t_c). The balance of diffusive and enhanced convection-driven ligand transport is defined by the local Peclet number, where $Pe_\delta = \dot{\gamma}_{(y=0)}d^2/D$. In this scenario, the growth of the depletion zone is halted at a steady state height δ depending on the rate of ligand replenishment. Additionally, past research has predicted that δ increases monotonically with increasing axial distance [59]. We hypothesize that this axial variation of δ leads to a heterogeneous delivery of ligand IgGs across the reaction site, ultimately influencing the homogeneity of ligand binding as observed in Section 4.5.2.

To validate this hypothesis, we performed numerical simulations using COMSOL, to examine the spatial evolution of δ across the reaction site for $2.7 \times 10^3 \leq Pe_\delta \leq 2.7 \times 10^7$. The device architecture, computational mesh geometries and the model definitions are elaborated in Section 4.4, which are consistent with the experimental conditions. Briefly, the 2-dimensional (2D) transport of ligand IgGs (where, $C_0 = 6.67 \text{ mol/m}^3$) was modelled by solving the coupled Navier-Stokes and convection-diffusion equation (equations 4.1, 4.2 & 4.6). The receptor–ligand IgG binding reaction was modelled on the reaction site, using the Langmuir adsorption model (equation 4.9 and boundary condition 4.11). As a limiting case, we modelled rapid irreversible surface reactions in COMSOL owing to the low rates of dissociation observed for IgG–IgG reactions ($k_{off} < 10^{-5} \text{ s}^{-1}$) [80, 81].

Figure 4.8a shows the 2D concentration profiles of ligand IgGs plotted against position along channel height, for low ($Pe_\delta = 2.7 \times 10^3$), moderate ($Pe_\delta = 2.7 \times 10^5$), and enhanced convective flows ($Pe_\delta = 2.7 \times 10^7$). The gradient of concentration profiles illustrate the depletion zone formed as a result of ligand IgG consumption at the reaction site. As seen in Figure 4.8a(i), a large depletion zone is formed in the confinement region, that extends downstream into the outlet channel. However, the depletion zone starts shrinking with increasing Pe_δ , illustrating that the ligand IgGs are efficiently replenished by the flowing fluid, following consumption at the reaction site.

Next, we investigated the influence of Pe_δ on the axial variation of depletion zone thickness across the reaction site. For this purpose, we plotted δ for varying positions across the reaction site at $50 \mu\text{m}$ intervals. The trailing and leading edges of the reaction site were omitted to avoid complications arising from edge effects. As seen in Figure 4.8b, δ was seen to increase with increasing distance from the leading area of the reaction site for $2.7 \times 10^3 \leq Pe_\delta \leq 2.7 \times 10^5$. With further increase in Pe_δ , the depletion zone was observed to be uniform across the reaction site, as illustrated by the invariance of δ on varying positions on the reaction site. The uniformity of δ implies that relatively equal concentrations of ligand IgGs are delivered to the entire surface of the reaction site. This subsequently results in a more homogeneous ligand binding. These results validate the hypothesis that the homogeneous ligand binding observed in Figure 4.7 is achieved when there is homogeneous ligand transport across the reaction site at large Pe_δ .

In addition, we observed a power law relationship between the mean depletion zone

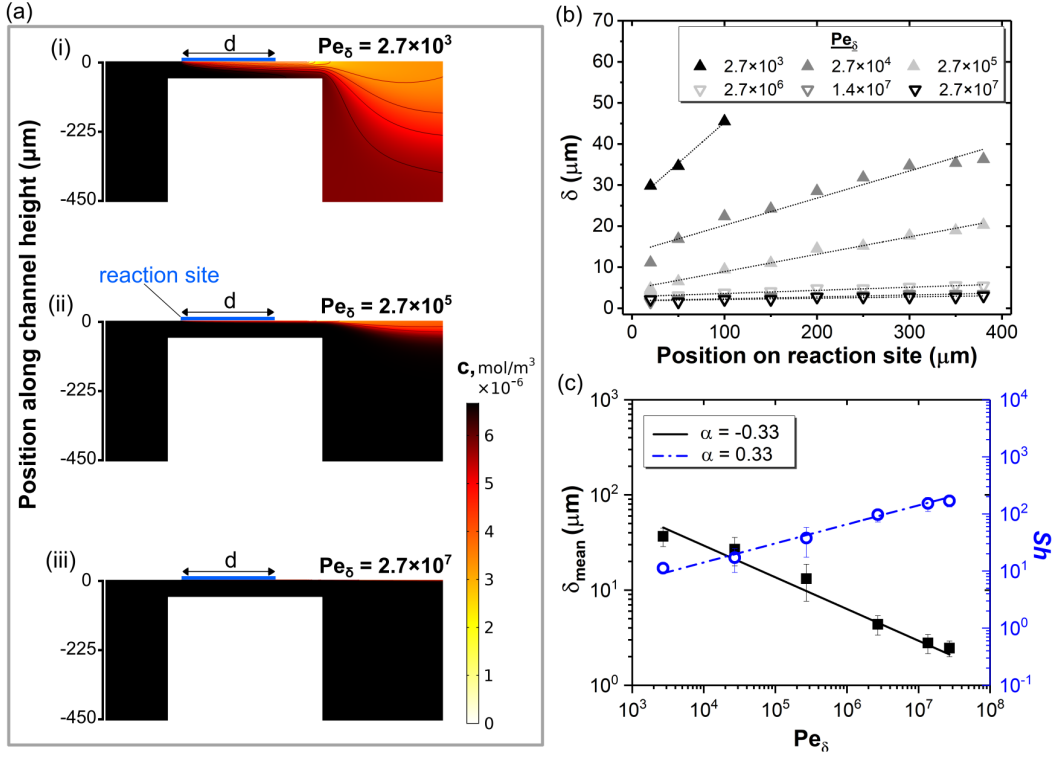


Figure 4.8: Relationship between Pe_δ and δ as observed by numerical simulations. (a) COMSOL simulations depicting the ligand depletion layer profiles in the confinement region of the 3D microchannel, for (i–iii) increasing Pe_δ . The gradient of ligand concentration (c) in the depletion zone is illustrated by the color scale, where the maximum concentration (black) is 6.67 mol/m^3 . (b) The depletion zone thickness at different positions of the reaction site centerline, plotted for increasing Pe_δ . Dotted lines are drawn to serve as linear trendlines for the plotted data. (c) The evolution of δ_{mean} with increasing Pe_δ is described by the power law, $\delta_{mean} \approx n(Pe_\delta)^\alpha$ (black symbols). Correspondingly, the Sherwood number (Sh) evolves with Pe_δ , as $Sh \approx (Pe_\delta)^\alpha$ (blue symbols). The trendlines depict the power laws for the respective plots.

thickness (δ_{mean}) and Pe_δ :

$$\delta_{mean} \approx \hat{d} \times (Pe_\delta)^\alpha, \quad (4.30)$$

where, $\alpha = -0.33$ and $\hat{d} = d \pm 232 \mu\text{m}$. It is worth noting that the variation of $\pm 232 \mu\text{m}$ from the analytically derived power law that defines $\hat{d} = d$ [59], was observed to be a result of the axial variations of δ across the reaction site.

Finally, we estimate the influence of Pe_δ on the ligand IgG transport flux using a dimensionless flux parameter, the Sherwood number (Sh). Here, Sh is defined as the ratio of diffusive (J_D) and enhanced convective flow-driven (J_δ) ligand flux rate perpendicular to the reaction site:

$$Sh \approx \frac{J_D}{J_\delta} \approx \frac{DC_0 d^2 / \delta}{DC_0 d} \approx \frac{d}{\delta}, \quad (4.31)$$

where, D is the ligand IgG diffusivity, C_0 is the initial ligand concentration, d is the length of the reaction site and δ is the depletion zone thickness. Figure 4.8c demonstrates that the Sherwood number (Sh) increases with increasing Pe_δ with the power law:

$$Sh \approx Pe_\delta^\alpha, \quad (4.32)$$

where, $\alpha = 0.33$, as predicted by the analytical solution proposed by Squires *et. al.*, [59]. The increase in Sh at $Pe_\delta > 10^5$ indicates that the replenishment of the ligand IgGs as they are consumed is controlled by local convection dominating close to the reaction site.

In the following sections, we perform in-depth investigations to understand how the receptor–ligand reaction kinetics transforms with enhanced convection-driven ligand IgG transport ($Sh > 10^1$ and $Pe_\delta > 10^5$).

4.5.4 Estimating the kinetic constants of the receptor–ligand IgG reaction

As the ligand IgGs diffuse across the depletion zone (δ) and reach the reaction site, they react with the receptor IgGs in a reversible fashion. This binding reaction is analytically described using the Langmuir adsorption model (equation 4.9) (refer to Section 4.5.2). To extract the kinetic constants, k_{on} and k_{off} , we monitored the receptor–ligand IgG binding kinetics at $Pe_\delta = 2.7 \times 10^7$, at sequentially increasing initial ligand IgG concentrations ($0.42 < C_0 < 13.33$ nM). Figure 4.9a depicts the evolution of fluorescence intensity ratios over a period of 40 mins for each C_0 , plotted as steps in the graph. Here, the fluorescence ratio is calculated as $I_{red}/(I_{red} + I_{green})$, where I_{red} and I_{green} are the median fluorescence intensities of the reaction site coated receptors bound with ligands (red) and coated with unbound receptors (green), respectively (see Figures 4.7a & c for reference).

We then temporally normalized the fluorescence intensity ratios for each C_0 by subtracting the fluorescence ratio at all time intervals (t) for a given C_0 , with the fluorescence ratio at time $t = 40$ mins for the preceding C_0 . This normalized fluorescence intensity ratio ultimately allowed us to estimate the fraction of bound receptors (f_B) for each case. The temporal evolution of f_B is plotted in Figure 4.9b for each C_0 . Each data set was fitted with equation 4.29 to extract the reaction equilibrium time, τ_R .

We plotted $1/\tau_R$ as a function of C_0 to yield a linear trend, as observed in Figure 4.9c. Finally, the kinetic constants k_{on} and k_{off} were obtained from the slope and intercept of the following linear fit equation:

$$\tau_R = (k_{on}C_0 + k_{off})^{-1}. \quad (4.33)$$

For the receptor–ligand IgG pairs used in this study, we obtained a k_{on} of $3.90 \times 10^5 M^{-1}s^{-1}$ and a k_{off} of $2.86 \times 10^{-4} s^{-1}$, at $Pe_\delta = 2.7 \times 10^7$. These kinetic constants are in agreement with the constants described in literature [81] for a moderate affinity polyclonal IgG pair. These kinetic constants are employed to investigate the receptor–ligand IgG reaction kinetics at $2.7 \times 10^5 < Pe_\delta < 2.7 \times 10^7$, in the following sections.

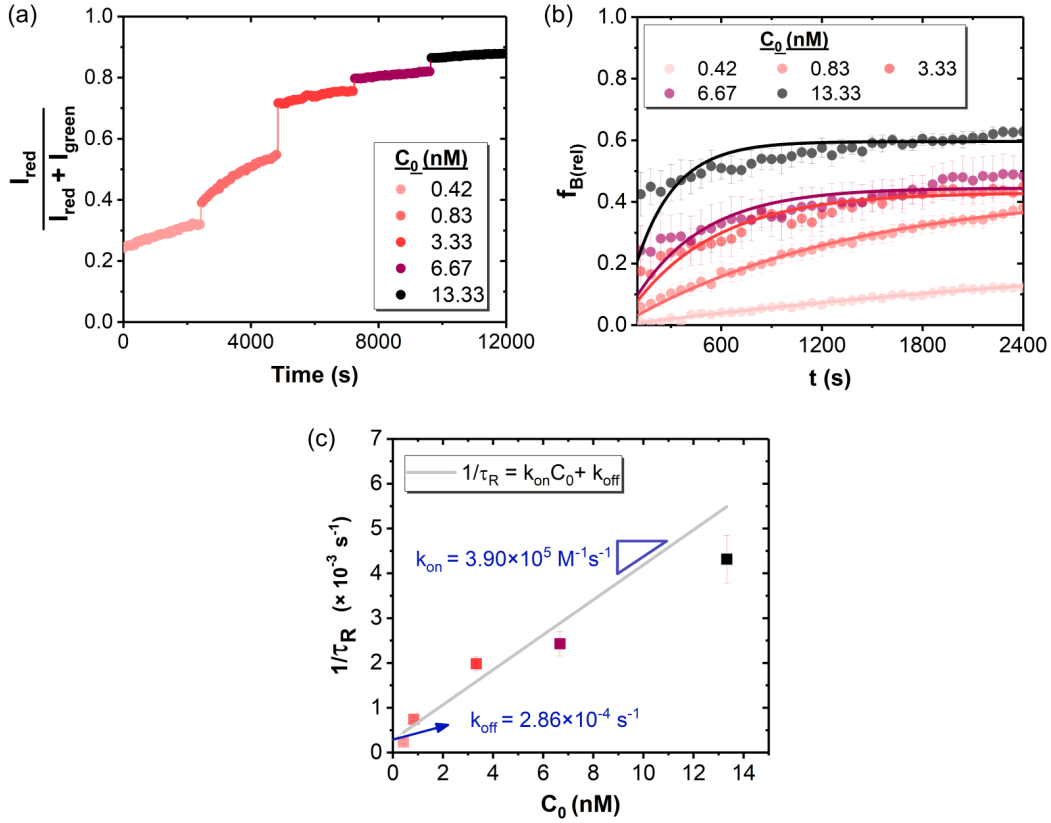


Figure 4.9: Ligand–receptor binding kinetics. (a) Evolution of fluorescent intensity ratio with time, depicting the binding of ligand IgG with receptor IgG for $Pe_\delta = 2.7 \times 10^7$. Each step of the curve indicates the IgG–IgG binding profile for serially increasing initial ligand IgG concentrations (C_0). (b) Fraction of bound receptor sites (f_B) plotted as a function of time for the respective C_0 introduced into the channel sequentially. Each data set is fitted with equation 4.29 to extract reaction equilibrium time (τ_R). (c) The reciprocal of τ_R is plotted against C_0 to obtain a linear profile, where the slope and intercepts of the curve generate the reaction rate constants, k_{on} and k_{off} , respectively. The grey line depicts the linear fit with equation 4.33. Error bars depicted in these figures are estimated from the standard deviations obtained for $n = 3$ datasets.

4.5.5 Re-examining the Damkohler number (Da) using kinetic scaling analysis

From the kinetic equation of the Langmuir adsorption model (equation 4.10), we know that the rate at which the ligands are captured by the receptors is heavily influenced by 3 important factors: (1) the kinetic constants (k_{on} and k_{off}) that define the affinity between the receptor and ligand IgGs, (2) the surface density of the receptors on the reaction site (b_{max}), and (3) the concentration of ligand IgGs close to the reaction site (c). Of these limiting factors, k_{on} , k_{off} can be tailored by bioengineering techniques and b_{max} can be optimized by surface chemistry techniques. Assuming that high affinity receptors are coated on the reaction site at high surface densities, the concentration of

ligands close to the reaction site (c) becomes the sole limiting factor that controls the speed of the receptor–ligand reaction.

As described in previous literature, convective replenishment of the consumed ligand and IgGs can play a dominant role in maintaining a steady supply of c close to the reaction site [59, 71]. Here, the balance between the ligand–receptor reaction rate and the rate of replenishment of c can be studied with the help of an important dimensionless parameter, the *Damkohler number* (Da). This dimensionless parameter naturally arises as a result of the nondimensional parametrization of the Langmuir kinetic equation (equation 4.10).

In Section 4.3.5, we employ conventionally used spatial and temporal scales as described by Gervais *et. al.* [58], and Squires *et. al.* [59] to derive $Da_{diffusion} = C_0 k_{on} \delta^2 / D$. Here, we assumed that the dominant time scale that influences the receptor–ligand reaction kinetics, is the time required for the ligand IgG to diffuse across the depletion zone ($t_\delta = \delta^2 / D$). As a result of this assumption, the time was scaled with t_δ to obtain the nondimensionalized time, $t^* = t / t_\delta = Dt / \delta^2$.

$Da_{diffusion}$ describes the balance between the three important phenomena competing for dominance at the reaction site: (1) receptor–ligand reaction kinetics (described by C_0 & k_{on}), (2) diffusion (described by D) and (3) enhanced convection-driven ligand IgG transport (described by δ). As per the definition, $Da_{diffusion} \gg 1$ implies that the time taken for the receptor–ligand reaction to reach equilibrium is determined by the time taken for the ligand IgGs to reach the reaction site. In this scenario, slow replenishment of c leads to a reduction in the ligand IgG capture rate. On the contrary, $Da_{diffusion} \ll 1$ implies that the equilibrium time is solely determined by the receptor–ligand reaction kinetics. In this ideal case, the ligand IgGs close to the reaction site are constantly replenished by the flowing carrier fluid, such that the capture of ligand IgGs is no longer affected by mass transport limitations.

As presented in Table 4.3, $Da_{diffusion} \ll 1$ for $Pe_\delta > 2.7 \times 10^5$, where $C_0 = 13.33$ nM, $k_{on} = 3.90 \times 10^5 M^{-1} s^{-1}$ and $k_{off} = 2.86 \times 10^{-4} s^{-1}$ for the receptor–ligand IgG pair used in this study. These low *Damkohler numbers* indicate that the ligand IgGs are efficiently replenished by the convecting flow as they are consumed, thereby removing mass transport limitations in this system.

To further strengthen this argument, we quantified the average concentration of ligand IgGs (\bar{c}) present in a $1 \mu\text{m}$ thick region close to the reaction site, from the numerical simulations elaborated in Section 4.5.3. We then plotted the ratio of \bar{c} / C_0 as a function of Pe_δ in Figure 4.10a. We observed an increasing \bar{c} / C_0 ratio with increasing

Table 4.3: Damkohler numbers employed in this study

Pe_δ	$Da_{diffusion}$	$Da_{kinetic}$
$(\dot{\gamma}_{(y=0)} d^2 / D)$	$(C_0 k_{on} \delta^2 / D)$	$(b_{max} k_{on} \delta / D)$
2.70×10^5	1.02×10^{-2}	1.17×10^{-1}
2.70×10^6	1.13×10^{-3}	3.87×10^{-2}
1.35×10^7	4.56×10^{-4}	2.46×10^{-2}
2.70×10^7	3.57×10^{-4}	2.18×10^{-2}

Pe_δ . In particular, we noticed that \bar{c} approaches C_0 (i.e., $\bar{c}/C_0 = 1$) at $Pe_\delta > 1.4 \times 10^7$, indicating that the ligand IgG concentration close to the reaction site is the same as the bulk ligand IgG concentration. This proves that the ligand IgGs are effectively replenished by the flowing carrier fluid as they are depleted by the reaction site, during strong convective flow.

Considering these observations, the time taken for the ligand IgGs to diffuse across δ is no longer the dominant time scale in this scenario, thereby invalidating the assumption employed in the nondimensionalization of the temporal scale (equation 4.21) used to derive $Da_{diffusion}$. To account for this deviation observed under enhanced convective flows, we hypothesize the speed of the ligand IgG detection is determined solely by the time taken for a ligand IgG molecule to react with a receptor IgG molecule at

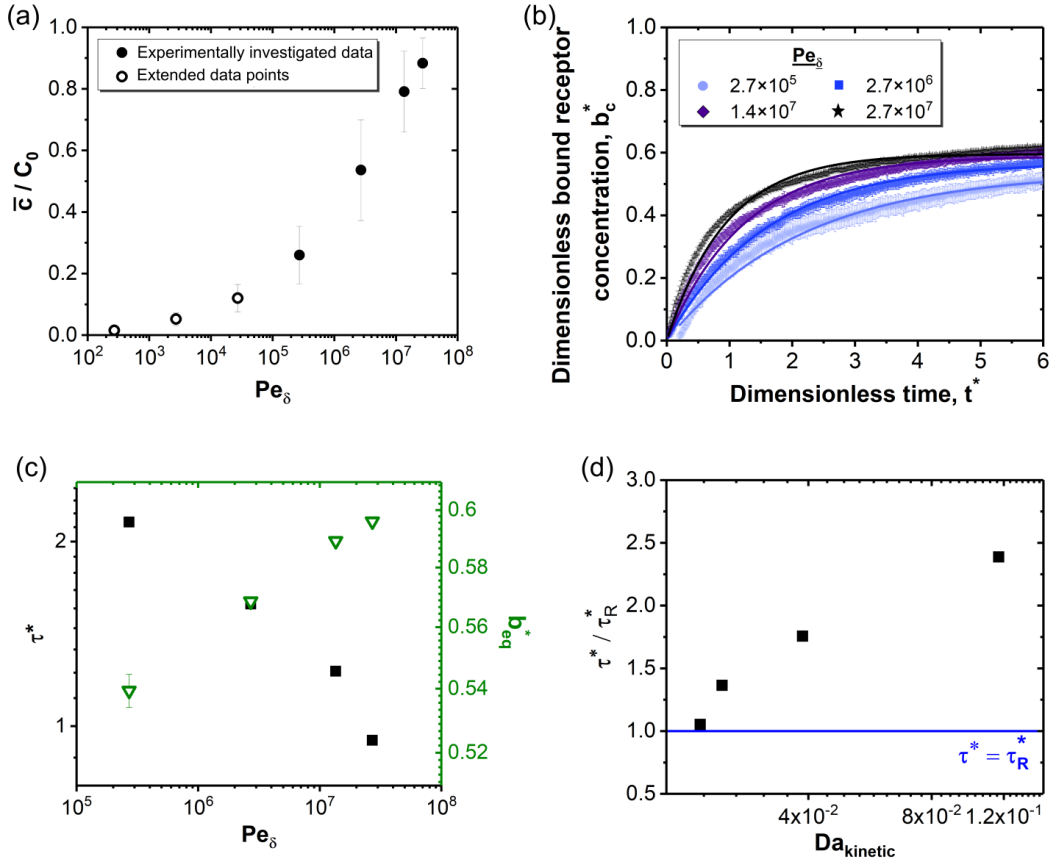


Figure 4.10: Ligand–receptor binding described by kinetic scaling analysis. (a) Ligand concentration close to reaction site (\bar{c}) extracted from the numerical simulations is scaled by the initial ligand concentration (C_0), and plotted as a function of Pe_δ . Closed symbols mark the experimentally investigated data and extended data points are plotted as open symbols. (b) Dimensionless bound receptor concentration ($b_c^* = b_c/b_{max}$) plotted as a function of dimensionless time ($t^* = k_{on}C_0t$). (c) Dimensionless reaction equilibrium time (τ^*) and dimensionless equilibrium bound receptor concentration (b_{eq}^*) plotted as a function of Pe_δ . (d) Dimensionless binding equilibration time (τ^*) normalized by dimensionless reaction time (τ_R^*) plotted as a function of kinetic Damkohler number ($Da_{kinetic}$). The blue line depicts the limit where $\tau^* = \tau_R^*$.

an “on-rate” of k_{on} . This results in a new dimensionless time scale, $t^* = t/t_{on} = C_0 k_{on} t$. Using this new temporal scale and the same spatial scales listed in equation 4.21, equation 4.10 is non-dimensionalized to obtain:

$$\frac{\partial b^*}{\partial t^*} = c^*(1 - b^*) - K_D^* b^*, \quad (4.34)$$

where, $K_D^* = k_{off}/(k_{on}C_0)$ is the non-dimensionalized kinetic dissociation coefficient.

Subsequently, the reaction-flux balance boundary condition (equation 4.11) is non-dimensionalized with the following scales:

$$b^* = \frac{b_c}{b_{max}}, \quad y^* = \frac{y}{\delta}, \quad t^* = C_0 k_{on} t, \quad (4.35)$$

to derive the scaled boundary condition,

$$\frac{\partial c^*}{\partial y^*} = -Da_{kinetic} [c^*(1 - b^*) - K_D^* b^*], \quad (4.36)$$

where, the $Da_{kinetic} = b_{max} k_{on} \delta / D$ is the *kinetic Damkohler number*. As seen in Table 4.3, $Da_{kinetic} \ll 1$ for $Pe_\delta > 2.7 \times 10^5$, indicating that mass transport conditions are overcome under these flow conditions. We employed $b_{max} = 1 \times 10^{-9}$ moles/m² (refer to Table 4.2), based on the assumption that 10% of receptor IgGs are able to capture ligand IgGs, when immobilized using APTES chemistry on glass surfaces (Section 4.2.2) [57].

It should be emphasized that both $Da_{kinetic}$ and $Da_{diffusion}$ provide the same information in this study. However, we propose that $Da_{kinetic}$ is more suitable to characterize the balance of receptor–ligand reaction rate and ligand transport rate, in scenarios where ligand transport is no longer a restriction, i.e., at $Pe_\delta \gg 10^5$.

In addition, as $c = C_0$ at $Pe_\delta \gg 10^5$, equation 4.34 can be analytically solved to obtain the following non-dimensional solution:

$$b_c^* = b_{eq}^* (1 - e^{-(t^*/\tau_R^*)}), \quad (4.37)$$

and,

$$\tau_R^* = (1 + K_D^*)^{-1}, \quad (4.38)$$

where, b_c^* and b_{eq}^* are the dimensionless bound receptor concentration at time= t^* and at equilibrium, respectively. τ_R^* is the dimensionless equilibrium reaction time. Equation 4.38 allows us to estimate the time taken for a given receptor–ligand reaction to reach equilibrium, based on the kinetic constants of the given receptor–ligand pair. Here, K_D^* can be estimated as $k_{off}/(k_{on}C_0)$.

Assuming that the speed of ligand detection is not influenced by mass transport limitations, the receptor–ligand IgG reaction can be estimated to reach equilibrium at a dimensionless equilibrium reaction time (τ_R^*) of 0.90, for an initial ligand IgG concentration of 13.33 nM, and kinetic constants $k_{on} = 3.90 \times 10^5 \text{ M}^{-1}\text{s}^{-1}$ and $k_{off} = 2.86 \times 10^{-4} \text{ s}^{-1}$.

To identify the time taken for receptor–ligand IgG reaction to equilibrate (τ^*) at varying Pe_δ , we plotted the evolution of b_c^* as a function of t^* for $2.7 \times 10^5 < Pe_\delta < 2.7 \times 10^7$, in Figure 4.10b, for $C_0 = 13.33$ nM. The data was fitted with equation 4.37 to extract τ^* and b_{eq}^* for each Pe_δ . As observed in Figure 4.10c, τ^* decreases for increasing Pe_δ (black squares). In addition, the reactions were seen to equilibrate at increasing equilibrium concentrations (b_{eq}^*) for increasing Pe_δ (green open triangles). These results demonstrate that enhanced convective ligand IgG transport enhances the receptor–ligand IgG reaction rate, thereby decreasing ligand IgG detection time.

Finally, we closely examine the influence of $Da_{kinetic}$ on τ^* in order to ascertain if this observed enhancement of receptor–ligand IgG reaction rate at increasing Pe_δ is a result of decreasing mass transport restrictions under these conditions. For this purpose we plotted the ratio of τ^*/τ_R^* as a function of $Da_{kinetic}$. As seen in Figure 4.10c, τ^* approaches τ_R^* ($\tau^*/\tau_R^* = 1$) at $Da_{kinetic} \ll 10^{-2}$, illustrating that the rate of ligand IgG delivery perfectly balances the receptor–ligand reaction, thereby reducing any delays in ligand IgG detection time that may arise from mass transport limitations.

In other words, the time taken for receptor–ligand IgG reaction to equilibrate under enhanced convective flows reaches the molecular reaction equilibrium time at $Pe_\delta \gg 10^7$. These results imply that the speed of the receptor–ligand reaction is no longer limited by the low abundance of ligand IgGs close to the vicinity of the reaction site, in this scenario. In other words, mass-transport limitations are terminated under these conditions, allowing for faster receptor–ligand reactions. Thus, rapid ligand detection can be achieved for any biomolecular system, by simply designing microfluidic devices that create strong convective flows given that, $Pe_\delta \gg 10^7$ for $Da_{kinetic} \ll 10^{-2}$.

4.5.6 Development of glass microfluidic bioassay devices with enhanced ligand detection speed and sensitivity

In the previous sections in this Chapter, we demonstrated that the homogeneity and “speed” of the receptor–ligand binding reactions can be enhanced by amplifying local ligand transport via convection. In this section, we explore the effect of Pe_δ on the ligand detection “sensitivity” of the 3D modular microfluidic devices. For this purpose, we monitored the real-time binding kinetics between the model receptor–ligand IgGs for a period of 20 mins for varying ligand concentrations (0.4 nM $< C_0 < 13.33$ nM), at $Pe_\delta = 2.7 \times 10^6$ & 2.7×10^7 .

In a typical bioassay system, it is more desirable to detect the reacting ligands as soon as the detector is able to capture the reaction signal, rather than waiting for the receptor–ligand reaction to equilibrate. In these cases, the ligand detection speed and sensitivity, i.e., the “detection efficiency”, strongly depends on (1) the total number of ligand molecules that bind at any given time, and (2) the ability of the detector to detect the capture ligands at that given time. To quantify the “detection efficiency” of the fluorescence-based 3D microfluidic bioassay devices, we first monitored the evolution of normalized median fluorescence intensity as a function of C_0 and Pe_δ , at a detection time of 10 mins. As seen in Figure 4.11a, the linear ligand IgG detection range starts at a lower C_0 for $Pe_\delta = 2.7 \times 10^7$ (red shaded region), when compared to $Pe_\delta = 2.7 \times 10^6$ (blue shaded region). Although the width of the linear ranges

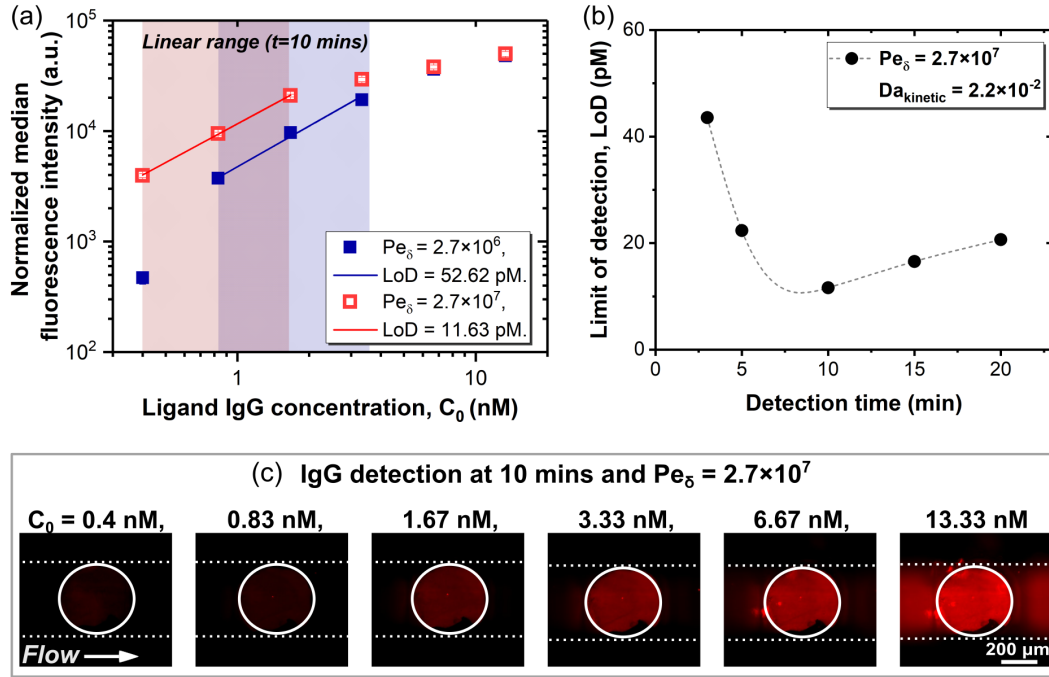


Figure 4.11: Influence of Pe_δ on limit of detection of ligand IgGs. (a) Ligand IgG concentration (C_0) plotted as a function of normalized median fluorescence intensity for $Pe_\delta = 2.7 \times 10^6$ & 2.7×10^7 , at time, $t = 10$ mins. The linear ranges are indicated by the red ($Pe_\delta = 2.7 \times 10^7$) and blue ($Pe_\delta = 2.7 \times 10^6$) shaded regions. The limit of detection (LoD) is estimated from the linear fit and equation 4.39 for each Pe_δ . $R^2 = 0.99$ for the linear fit and the error bars ($n = 9$) are within the symbols. (b) The variations in LoD as a function of detection time are plotted following calculations for the same C_0 range for $Pe_\delta = 2.7 \times 10^7$ and $Da_{kinetic} = 2.2 \times 10^{-2}$. The dotted spline is used to illustrate the general trend of the data. (c) Fluorescence micrographs depicting the reaction site after capture of ligand IgGs at 10 mins, for the C_0 range used in the LoD calculations in (b). The dotted lines illustrate the microchannel boundaries and the white circles delineate the reaction site.

were observed to be similar, the starting concentration for the linear range was seen to increase by a factor of 2 when Pe_δ was reduced by one order of magnitude. These observations indicate that the total number of ligand IgGs that reach the reaction site in 10 mins is lower for $Pe_\delta = 2.7 \times 10^6$ than $Pe_\delta = 2.7 \times 10^7$. Furthermore, the depletion zone thickness δ was estimated to be a factor of 2 smaller for $Pe_\delta = 2.7 \times 10^7$ ($\delta = 2.4 \mu\text{m}$) than $Pe_\delta = 2.7 \times 10^6$ ($\delta = 4.5 \mu\text{m}$), as seen in the numerical simulations described in Section 4.5.3. As a consequence, at lower Pe_δ , (1) the ligand IgGs have to diffuse across a larger distance to reach the reaction site, and (2) the consumed ligand IgGs are replenished at a slower rate close to the reaction site. These two factors cumulatively both decrease the total number of ligand IgGs detected at any given time and increase the ligand detection time at low Pe_δ .

In addition, the “sensitivity” of the 3D microfluidic bioassay device was quantified by calculating the limit of detection (LoD) from the linear fit Figure 4.11a and the

following equation [83]:

$$LoD = 3.3(SD_{(int)}/s), \quad (4.39)$$

where, $SD_{(int)}$ and s are the standard deviations of the y-intercept and the slopes of the linear fit, respectively (red and blue solid lines in Figure 4.11a). At a detection time of 10 mins, the LoD was seen to be ≈ 5 -fold lower for $Pe_\delta = 2.7 \times 10^7$ (LoD=11.63 pM), when compared to that of $Pe_\delta = 2.7 \times 10^6$ (LoD=52.62 pM). This reduction in LoD at high Pe_δ further demonstrates the ability of enhanced local convective flows to improve the ligand detection “sensitivity” of microfluidic bioassay systems.

Upon further examinations, we observed that low concentrations of ligand IgGs ($C_0 < 1$ nM) could be fluorescently detected within 5 mins using the 3D modular microfluidic bioassay system, at $Pe_\delta = 2.7 \times 10^7$. As illustrated in Figure 4.11b, the LoD of the system was quantified to be highest at a detection time of 3 mins (LoD=43.33 pM) and steadily decreased upto 10 mins (LoD=11.63 pM). A gradual increase in LoD was observed at detection times larger than 15 mins. This gradual increase is attributed to the (1) decreasing linearity of the receptor–ligand kinetic curve as the reaction gradually approaches equilibrium ($\tau_R \approx 7$ mins), and (2) increasing errors in median fluorescence intensity due to formation of aggregates at large Pe_δ .

Consequently, these results demonstrate that high “detection efficiency” fluorescence based microfluidic bioassay systems can be fabricated to detect a wide range of ligand IgG concentrations (Figure 4.11c) “rapidly” (detection time of 10 mins) and with high “sensitivity” (LoD=11.63 pM), using the proposed design principles (i.e., $Pe_\delta \gg 10^7$ for $Da_{kinetic} \ll 10^{-2}$).

4.5.7 Collective influence of Pe_δ on receptor–ligand reaction kinetics

The design rules proposed in the previous sections are in agreement with the rules proposed by previous authors [26, 58, 59], where the rules were all based on a very important assumption: the maximum attainable reaction speed in any system is defined by the molecular properties of the receptor–ligand pairs, vis-à-vis the kinetic constants. These assumptions were based on another important assumption that the kinetic constants, i.e., k_{on} and k_{off} , are invariant of external factors such as flow, temperature, ionic strength, etc.

Given that the addition of variable ionic strength and temperature would add further complexity to the models used to describe microfluidic bioassay systems, we wanted to explore the effects of a less complex variable i.e., shear rate, on the variance of reaction kinetic constants. In addition to being an easily altered variable, shear rate ($\dot{\gamma}_{(y=0)}$) is already incorporated in the analytical model by means of the local Peclet number, Pe_δ .

Using the same set of IgGs as described above, we performed receptor–ligand reaction kinetic experiments, at two different Pe_δ . Here, we plotted the temporal change of f_B (fraction of bound receptors) in Figures 4.12a(i) & b(i) for variable C_0 , at $Pe_\delta = 2.7 \times 10^6$ and $Pe_\delta = 2.7 \times 10^7$, respectively. Each data set was fitted with equation 4.29 to extract the reaction equilibrium time, τ_R . We extracted the kinetic

constants k_{on} and k_{off} from the slope and intercept of the linear fit in the plots of $1/\tau_R$ vs C_0 , for $Pe_\delta = 2.7 \times 10^6$ and $Pe_\delta = 2.7 \times 10^7$, as observed in Figures 4.12a(ii) & b(ii).

For the same receptor–ligand IgG pairs used in this study, we observed a significant difference in k_{on} and k_{off} values for the two Pe_δ . As seen in Table 4.4, while the changes in k_{on} with increasing Pe_δ were observed to be minute, an order-of-magnitude increase in k_{off} was observed with a proportional order-of-magnitude increase in Pe_δ .

These results indicate that while the association reaction between the receptor and ligand remain unchanged, the dissociation reaction is accelerated with increasing local convection close to the reaction site surface. Prior literature reported similar

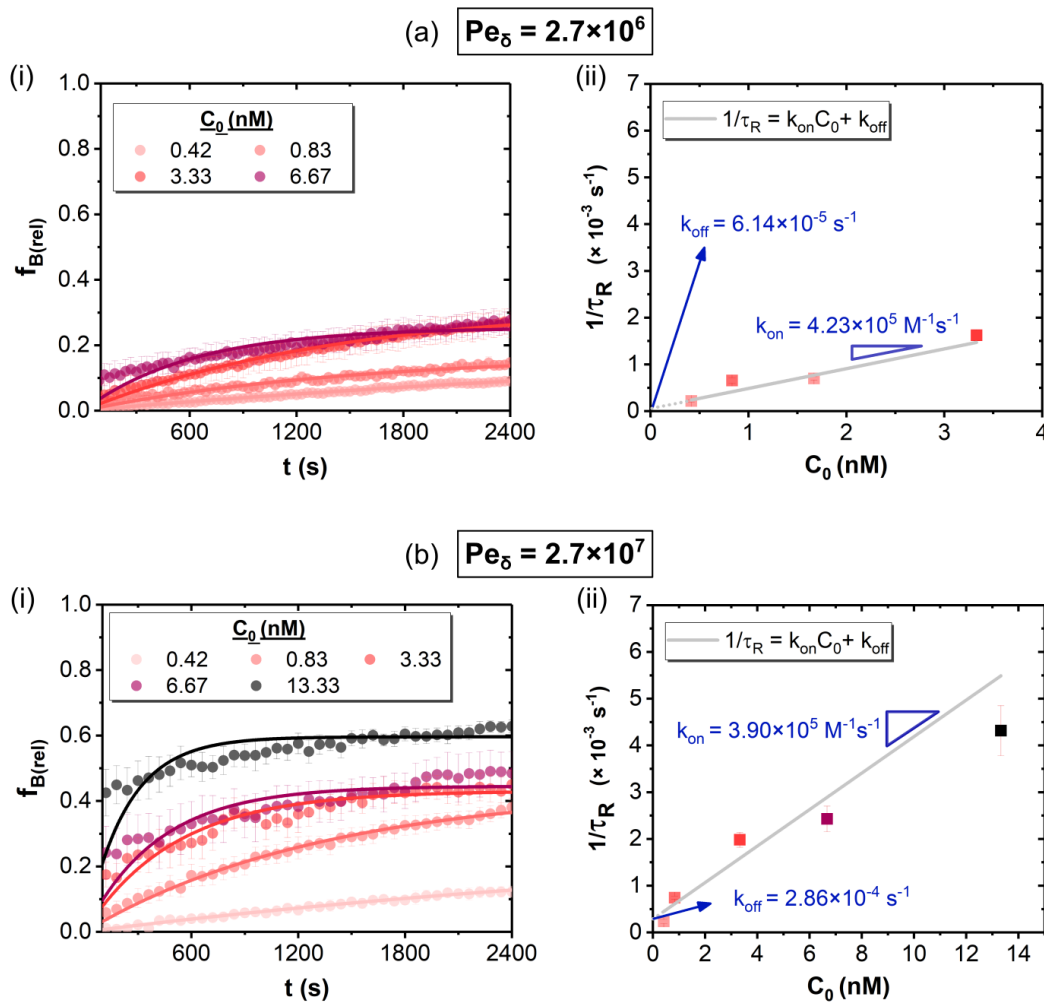


Figure 4.12: Influence of Pe_δ on kinetic constants. Fraction of bound receptor sites (f_B) plotted as a function of time for the respective C_0 introduced into the channel sequentially, for (a)(i) $Pe_\delta = 2.7 \times 10^6$ & (b)(i) $Pe_\delta = 2.7 \times 10^7$. Each data set is fitted with equation 4.29 to extract reaction equilibrium time (τ_R). The reciprocal of τ_R is plotted against C_0 to obtain a linear profile for (a)(ii) $Pe_\delta = 2.7 \times 10^6$ & (b)(ii) $Pe_\delta = 2.7 \times 10^7$. Here, the slope and intercepts of the curve generate the kinetic constants, k_{on} and k_{off} , respectively. The grey line depicts the linear fit with equation 4.33.

Table 4.4: Kinetic constants observed at variable Pe_δ

Pe_δ	k_{on}	k_{off}
$(\dot{\gamma}_{(y=0)}d^2/D)$	$(M^{-1}s^{-1})$	(s^{-1})
2.70×10^6	4.23×10^5	6.14×10^{-5}
2.70×10^7	3.90×10^5	2.86×10^{-4}

observations in studies focussed on understanding the effect of shear stress on cell–receptor adhesion in biological systems [84, 85] and receptor–ligand reactions in the BIAcore biosensing system [86].

However, the analytical models that have been derived to describe the receptor–ligand binding reactions in microfluidic systems, fail to account for this proportional relationship between k_{off} and Pe_δ . By solely relying on the design rules that suggest the fabrication of fast flow systems, we are neglecting the effects of enhanced dissociation of captured ligands at increasing shear rates. While this could be seen as a potential drawback of enhanced convective flows, it is worth noting that the dissociated ligands are also simultaneously replenished as a consequence of the fast transport, thereby creating a self-sustaining feedback loop.

Although the effects of enhanced k_{off} at large Pe_δ may not have a detrimental impact on the speed of the receptor–ligand sensing systems, it plays a major role in applications where microfluidic systems are exploited to quantify the kinetic constants [87, 88]. Due to the high variability of k_{off} at high flow rates, utmost care must be taken before interpreting the kinetic parameters. While this observation was noted only at high flow rates, it is unclear if the variability of the kinetic constants can be prevented by employing slow flow rates. Additionally, further research is required to be able to include this flow rate-dependent variation of k_{off} in the analytical models used to describe microfluidic receptor–ligand binding reactions. Furthermore, these preliminary observations open doors for further investigations in the future.

4.6 Conclusions

In this chapter, we described a novel method to fabricate modular 3D microfluidic bioassay devices using selective laser etching process enabled by the LightFab 3D printer. The fabricated device consists of an embedded 3D microfluidic channel that locks with a conical component patterned with receptor molecules using the previously described microcontact printing strategy described in Chapter 3.

Using these devices, we studied the binding kinetics between model receptor–ligand IgG molecules under enhanced convective flows. We proposed scaling solutions to present important dimensionless parameters that could be used to study the balance of competing phenomena in this system. These parameters are listed in Table 4.5.

We observed that homogeneous ligand binding across the reaction site can be achieved by creating a thin and uniform depletion layer with enhanced local convection (i.e., $Sh > 10^1$ & $Pe_\delta \gg 10^5$). Additionally, we demonstrated that the mass transport limitations are overcome with enhanced convective ligand transport, thereby enhancing

Table 4.5: Dimensionless parameters employed in this study

Dimensionless parameter	Definition	Significance
$\beta = h/d$	dimensionless aspect ratio	$\frac{\text{confinement height}}{\text{reaction site length}}$
$Pe_h = Q/wD$	bulk Peclet number	$\frac{\text{convection rate}}{\text{diffusion rate}}$
$Pe_\delta = \dot{\gamma}_{(y=0)}d^2/D$	local Peclet number	$\frac{\text{shear rate}}{\text{diffusion rate}}$
$Sh = d/\delta$	Sherwood number	$\frac{\text{diffusive flux rate}}{\text{convective flux rate}}$
$Da_{diffusion} = C_0k_{on}\delta^2/D$	diffusion Damkohler no.	$\frac{\text{reaction rate}}{\text{mass transport rate}}$
$Da_{kinetic} = b_{max}k_{on}\delta/D$	kinetic Damkohler no.	$\frac{\text{reaction rate}}{\text{mass transport rate}}$
$K_D^* = b_{max}k_{on}\delta/D$	dimensionless dissociation constant	$\frac{\text{ligand dissociation rate}}{\text{ligand association rate}}$

the speed of the receptor–ligand binding reaction. We subsequently proposed kinetic scaling analysis method to derive $Da_{kinetic}$, that can be used to characterize enhanced convective flow receptor–ligand reaction systems more reliably than the conventional $Da_{diffusion}$ obtained by diffusion scaling analysis. Using the observed results, we proposed design rules that enabled the fabricate enhanced microfluidic receptor–ligand IgG bioassay systems with a limit of detection of 11.63 pM (1.75 ng/ml) and detection speed of 10 mins. Finally, we presented preliminary data that shows the increase in dissociation constant, k_{off} at high flow rates.

These results not only provides comprehensive analyses to allow users to design rapid biosensing systems for different biomolecules (not limited to IgGs), but also pave way for further interesting investigations in the future.

Conclusions and Future Perspectives

The aim of this thesis was to propose design principles for the development of rapid, sensitive and user-friendly point-of-care (POC) disease diagnostic devices. To this end, a manually-operated proof-of-concept POC testing device was developed by integrating novel fluid handling modules with simple polymethyl methacrylate (PMMA) microfluidic bioassay devices. To tune the speed and sensitivity of the developed microfluidic bioassay systems, flow-dependent kinetic enhancement investigations were carried out. This concluding section summarizes the findings reported in each chapter of this thesis.

Chapter 2

A simple and rapid method to fabricate efficient PMMA microfluidic bioassay devices at high-throughput was proposed in Chapter 1. First, we exploited radio-frequency (RF) air plasma to generate functional groups that enabled the subsequent covalent coupling of receptor proteins on PMMA surfaces. We observed that the plasma energy had a direct influence on the density of polar and hydrophobic groups generated on the PMMA surfaces. A maximum density of carboxyl groups (*COOH*) could be obtained on the PMMA surface when exposed to 27 kJ of air plasma. At these optimum conditions, the *COOH*-rich PMMA surfaces showed the highest affinity towards green fluorescent protein (GFP), when coupled via EDC-NHS mediated chemistry.

Additionally, high GFP surface densities could be obtained with lower initial concentrations of GFP at a neutral pH of 7.4. The immobilized GFP molecules retained their bio-functionalities, depicted by their ability to serve as receptors that captured GFP-specific ligand immunoglobulin G molecules (IgGs). This demonstrated functionalization strategy is applicable to a wide range of receptor molecules, namely, IgGs, streptavidin and major outer membrane proteins (MOMP) of *Chlamydia trachomatis*. Finally, microfluidic antibody assay devices were fabricated to detect clinically significant concentrations of *Chlamydia trachomatis* specific antibodies.

While polymeric substrates are most commonly used to manufacture microfluidic bioassay devices at large-scale, the inert nature of these materials has resulted in the need to use stringent surface functionalization strategies for the immobilization of receptor molecules. The fabrication strategy discussed in this chapter paves way to create high-throughput PMMA microfluidic bioassay using rapid and scalable, yet controlled bio-functionalization methods, without causing any changes in the functionalities of immobilized biomolecules or the PMMA surfaces.

Chapter 3

In Chapter 2, the developed PMMA microfluidic bioassay devices were integrated with a modular Fluid Handling Device (FHD) to serve as a “proof-of-concept” manually operated point-of-care (POC) testing device for the detection of *Chlamydia trachomatis* specific IgGs.

The manually-powered FHD module allowed the user to process a deposited sample by mixing it with on-board stored reagents, filtering the mixture and delivering it to subsequent modules. The FHD was developed to be used as a stand-alone fluid processing system or used to couple with the microfluidic bioassay chip for disease detection. The integrated system with coupled FHD and PMMA microfluidic bioassay devices enabled the detection of *Chlamydia trachomatis* specific IgG from a buffer-based blood mimic sample, with a limit of detection of 1.05 $\mu\text{g}/\text{ml}$ within 15 mins. The high limit of detection was observed to be a result of suboptimal design of the developed PMMA microfluidic bioassay devices. Nevertheless, the existing prototype was shown to be completely integrated, easy to use, hand-held, manually powered and disposable, with the potential of serving as a point-of-care testing device.

In the following chapters, we investigated the parameters that influenced the roots of these issues. Here, we focussed on developing glass-based microfluidic bioassay systems (1) to eliminate contributions of fluorescence scattering, (2) to allow for fabrication of robust microfluidic devices (3) that served as a better model system to study receptor–ligand binding kinetics at high flow rates.

Chapter 4

In this chapter, we demonstrated a 2-step microcontact printing approach to encapsulate covalently immobilized receptor molecules within glass-based microfluidic bioassay devices. First, micropatterns of (3-aminopropyl)triethoxysilane (APTES), an amine $-\text{NH}_2$ terminated silane, were transferred from an elastomeric polydimethylsiloxane (PDMS) stamp to a hydrophilic glass surface, by microcontact printing. During this process, we replaced conventional solvents (toluene and ethanol) with water to limit the diffusion of APTES within the PDMS stamp, thereby allowing us to create micro- and nanoscale microcontact printed features. These APTES patterned surfaces were observed to be stable for up to 3 months post printing.

The APTES patterned substrates were bonded to open-ended microfluidic channels to complete the device. Receptor molecules such as IgGs and DNA aptamers were coupled to APTES within the channels using standard EDC–NHS chemistry or BS3 chemistry. Using dispensing robots and microfluidic channel networks, we demonstrated the ability of functionalizing multiple kinds of receptor molecules within one device using just on stamping process. Finally, by coupling the receptor molecules immediately prior to use, the bio-functionalities of the receptors were observed to be well preserved, while maintaining their ability to bind to biomarkers such as C-reactive protein (CRP) and interleukin 6 (IL6).

Chapter 5

In the final chapter, we used this simple patterning technique to immobilize receptor IgGs onto fused silica substrates to create truly 3D microfluidic channels. These 3D microfluidic channels were fabricated using a relatively new selective laser etching process enabled by the LightFab 3D printer. We used these devices to experimentally

investigate the influence of enhanced convective flows on the binding kinetics between complementary receptor–ligand IgGs.

We re-examined the scaling analyses proposed in prior literature to experimentally validate the assumptions made for the scaling processes. First, we defined the local Peclet number $Pe_\delta = \dot{\gamma}d^2/D$ that helped us characterize the balance between local convection and diffusion driven transport of ligands within the microfluidic devices. At $Pe_\delta \gg 10^5$, homogeneous binding of ligands across the reaction site surface was observed. This observation was explained to be a result of the uniform thinning of the depletion zone, (ligand concentration gradient created as a result of steady binding with receptors at the reaction site) at high Pe_δ . Additionally, under these conditions, a steady replenishment of ligands close to the reaction site was observed to enhance the receptor–ligand reaction kinetics.

Using kinetic scaling analysis, we proposed the use of the kinetic Damkohler number ($Da_{kinetic} = b_{max}k_{on}\delta/D$) to characterize the balance between the rates of receptor–ligand binding and enhanced convection-driven ligand replenishment. Finally we proposed that rapid ligand detection can be achieved for any biomolecular system by designing microfluidic devices with $Pe_\delta \gg 10^7$ for $Da_{kinetic} \ll 10^{-2}$. Using the proposed design rules, we fabricated high sensitivity (LoD=1.75 ng/ml) and high speed (detection speed of 10 mins) fluorescence-based glass microfluidic IgG-detection systems. By applying these design principles to the integrated FHD–microfluidic POC system, we envision the creation of highly efficient point-of-care testing systems in the future. In addition, we observed an apparent increase in the kinetic dissociation constant (k_{off}) of receptor–ligand IgG reactions at increasing Pe_δ . If proven definitively, these observations have immense implications in applications where microfluidic systems are used to quantify kinetic constants in biomolecular systems.

The results presented in this thesis not only serve as design references for the fabrication of rapid and sensitive point-of-care testing systems, but also present interesting observations that open doors for further comprehensive studies in the future. In addition, the novel 3D modular glass microfluidic devices developed in this thesis could serve as robust platforms to obtain new insights in transport phenomena and reaction kinetics at small length scales.

Bibliography

- [1] S. Sathish, K. Toda-Peters, and A. Q. Shen, “Proof-of-concept modular fluid handling prototype integrated with microfluidic biochemical assay modules for point-of-care testing,” *View*, vol. 1, no. 1, p. e1, 2020.
- [2] S. Sathish, N. Ishizu, and A. Q. Shen, “Air plasma-enhanced covalent functionalization of poly (methyl methacrylate): high-throughput protein immobilization for miniaturized bioassays,” *ACS Applied Materials & Interfaces*, vol. 11, no. 49, pp. 46350–46360, 2019.
- [3] K. Toda-Peters, A. Q. Shen, S. Sathish, D. Lee, C. J. Galvin, and K. Funakoshi, “Integrated system for sampling and processing a liquid suspension,” Okinawa Institute of Science and Technology Graduate University, US Patent WO2018216607A1, 2018.
- [4] S. Sathish, S. G. Ricoult, K. Toda-Peters, and A. Q. Shen, “Microcontact printing with aminosilanes: creating biomolecule micro- and nanoarrays for multiplexed microfluidic bioassays,” *Analyst*, vol. 142, no. 10, pp. 1772–1781, 2017.
- [5] A. K. Yetisen, M. S. Akram, and C. R. Lowe, “based microfluidic point-of-care diagnostic devices,” *Lab on a Chip*, vol. 13, no. 12, pp. 2210–2251, 2013.
- [6] C. H. Jones, J. Howick, N. W. Roberts, C. P. Price, C. Heneghan, A. Plüddemann, and M. Thompson, “Primary care clinicians’ attitudes towards point-of-care blood testing: a systematic review of qualitative studies,” *BMC Family Practice*, vol. 14, no. 1, p. 117, 2013.
- [7] H. Chen, K. Liu, Z. Li, and P. Wang, “Point of care testing for infectious diseases,” *Clinica Chimica Acta*, vol. 493, pp. 138–147, 2019.
- [8] A. Qureshi, Y. Gurbuz, and J. H. Niazi, “Biosensors for cardiac biomarkers detection: A review,” *Sensors and Actuators B: Chemical*, vol. 171, pp. 62–76, 2012.
- [9] S. Kc, X. Z. Wang, and J. E. Gallagher, “Diagnostic sensitivity and specificity of host-derived salivary biomarkers in periodontal disease amongst adults: Systematic review,” *Journal of Clinical Periodontology*, vol. 47, no. 3, pp. 289–308, 2020.
- [10] S. Hutt, A. Tailor, P. Ellis, A. Michael, S. Butler-Manuel, and J. Chatterjee, “The role of biomarkers in endometrial cancer and hyperplasia: a literature review,” *Acta Oncologica*, vol. 58, no. 3, pp. 342–352, 2019.

- [11] F. Li, M. You, S. Li, J. Hu, C. Liu, Y. Gong, H. Yang, and F. Xu, “based point-of-care immunoassays: Recent advances and emerging trends,” *Biotechnology Advances*, vol. 39, p. 107442, 2020.
- [12] B. Dai, S. Chen, W. Li, L. Zheng, X. Han, Y. Fu, J. Wu, F. Lin, D. Zhang, and S. Zhuang, “Fully-functional semi-automated microfluidic immunoassay platform for quantitation of multiple samples,” *Sensors and Actuators B: Chemical*, vol. 300, p. 127017, 2019.
- [13] Q. Lin, D. Wen, J. Wu, L. Liu, W. Wu, X. Fang, and J. Kong, “Microfluidic immunoassays for sensitive and simultaneous detection of IgG/IgM/antigen of SARS-CoV-2 within 15 min,” *Analytical Chemistry*, vol. 92, no. 14, pp. 9454–9458, 2020.
- [14] S. T. Sanjay, M. Li, W. Zhou, X. Li, and X. Li, “A reusable PMMA/paper hybrid plug-and-play microfluidic device for an ultrasensitive immunoassay with a wide dynamic range,” *Microsystems & Nanoengineering*, vol. 6, no. 1, pp. 1–11, 2020.
- [15] T. Fujii, “PDMS-based microfluidic devices for biomedical applications,” *Microelectronic Engineering*, vol. 61, pp. 907–914, 2002.
- [16] S. K. Sia and G. M. Whitesides, “Microfluidic devices fabricated in poly (dimethylsiloxane) for biological studies,” *Electrophoresis*, vol. 24, no. 21, pp. 3563–3576, 2003.
- [17] N. Burshtein, S. T. Chan, K. Toda-Peters, A. Q. Shen, and S. J. Haward, “3D-printed glass microfluidics for fluid dynamics and rheology,” *Current Opinion in Colloid & Interface Science*, vol. 43, pp. 1–14, 2019.
- [18] H. Becker and L. E. Locascio, “Polymer microfluidic devices,” *Talanta*, vol. 56, no. 2, pp. 267–287, 2002.
- [19] K. Liu and Z. H. Fan, “Thermoplastic microfluidic devices and their applications in protein and DNA analysis,” *Analyst*, vol. 136, no. 7, pp. 1288–1297, 2011.
- [20] D. Mark, S. Haeberle, G. Roth, F. von Stetten, and R. Zengerle, “Microfluidic lab-on-a-chip platforms: requirements, characteristics and applications,” *Chemical Society Reviews*, vol. 39, no. 3, pp. 1153–1182, 2010.
- [21] M. Karle, S. K. Vashist, R. Zengerle, and F. von Stetten, “Microfluidic solutions enabling continuous processing and monitoring of biological samples: A review,” *Analytica Chimica Acta*, vol. 929, pp. 1–22, 2016.
- [22] J. C. Slattery, *Advanced transport phenomena*. Cambridge University Press, 1999.
- [23] A. H. Ng, U. Uddayasankar, and A. R. Wheeler, “Immunoassays in microfluidic systems,” *Analytical and Bioanalytical Chemistry*, vol. 397, no. 3, pp. 991–1007, 2010.

-
- [24] S. Tombelli, M. Minunni, and M. Mascini, "Analytical applications of aptamers," *Biosensors and Bioelectronics*, vol. 20, no. 12, pp. 2424–2434, 2005.
- [25] M. D. Tarn and N. Pamme, "Microfluidic platforms for performing surface-based clinical assays," *Expert Review of Molecular Diagnostics*, vol. 11, no. 7, pp. 711–720, 2011.
- [26] M. Zimmermann, E. Delamarche, M. Wolf, and P. Hunziker, "Modeling and optimization of high-sensitivity, low-volume microfluidic-based surface immunoassays," *Biomedical Microdevices*, vol. 7, no. 2, pp. 99–110, 2005.
- [27] E. Gizeli and C. R. Lowe, *Biomolecular sensors*. CRC Press, 2003.
- [28] G. T. Hermanson, *Bioconjugate techniques*. Academic Press, 2013.
- [29] S. K. Vashist, "Comparison of 1-ethyl-3-(3-dimethylaminopropyl) carbodiimide based strategies to crosslink antibodies on amine-functionalized platforms for immunodiagnostic applications," *Diagnostics*, vol. 2, no. 3, pp. 23–33, 2012.
- [30] M. G. Sarngadharan, R. Pal, and A. L. DeVico, "Antibodies to crosslinkers and methods for using the same," Biomerieux Incorporation, US Patent US6503736B1, 2003.
- [31] A. K. Trilling, J. Beekwilder, and H. Zuilhof, "Antibody orientation on biosensor surfaces: a minireview," *Analyst*, vol. 138, no. 6, pp. 1619–1627, 2013.
- [32] B. Saha, T. H. Evers, and M. W. Prins, "How antibody surface coverage on nanoparticles determines the activity and kinetics of antigen capturing for biosensing," *Analytical Chemistry*, vol. 86, no. 16, pp. 8158–8166, 2014.
- [33] E. E. Hui and S. N. Bhatia, "Microscale control of cell contact and spacing via three-component surface patterning," *Langmuir*, vol. 23, no. 8, pp. 4103–4107, 2007.
- [34] J. L. Garcia-Cordero and S. J. Maerkl, "Multiplexed surface micropatterning of proteins with a pressure-modulated microfluidic button-membrane," *Chemical Communications*, vol. 49, no. 13, pp. 1264–1266, 2013.
- [35] M. A. Ray, N. Shewmon, S. Bhawalkar, L. Jia, Y. Yang, and E. S. Daniels, "Sub-micrometer surface patterning using interfacial colloidal particle self-assembly," *Langmuir*, vol. 25, no. 13, pp. 7265–7270, 2009.
- [36] M. Mrksich and G. M. Whitesides, "Patterning self-assembled monolayers using microcontact printing: a new technology for biosensors?," *Trends in Biotechnology*, vol. 13, no. 6, pp. 228–235, 1995.
- [37] L. Filipponi, P. Livingston, O. Kašpar, V. Tokárová, and D. V. Nicolau, "Protein patterning by microcontact printing using pyramidal PDMS stamps," *Biomedical Microdevices*, vol. 18, no. 1, pp. 1–7, 2016.

- [38] R. Castagna, A. Bertucci, E. A. Prasetyanto, M. Monticelli, D. V. Conca, M. Massetti, P. P. Sharma, F. Damin, M. Chiari, L. De Cola, *et al.*, “Reactive microcontact printing of DNA probes on (DMA-NAS-MAPS) copolymer-coated substrates for efficient hybridization platforms,” *Langmuir*, vol. 32, no. 13, pp. 3308–3313, 2016.
- [39] R. S. Kane, S. Takayama, E. Ostuni, D. E. Ingber, and G. M. Whitesides, “Patterning proteins and cells using soft lithography,” *Biomaterials*, vol. 20, no. 23, pp. 2363–2376, 1999.
- [40] E. B. Chakra, B. Hannes, J. Vieillard, C. D. Mansfield, R. Mazurczyk, A. Bouchard, J. Potempa, S. Krawczyk, and M. Cabrera, “Grafting of antibodies inside integrated microfluidic–microoptic devices by means of automated microcontact printing,” *Sensors and Actuators B: Chemical*, vol. 140, no. 1, pp. 278–286, 2009.
- [41] W. Norde, “My voyage of discovery to proteins in flatland . . . and beyond,” *Colloids and Surfaces B: Biointerfaces*, vol. 61, no. 1, pp. 1–9, 2008.
- [42] Z.-H. Wang and G. Jin, “Silicon surface modification with a mixed silanes layer to immobilize proteins for biosensor with imaging ellipsometry,” *Colloids and Surfaces B: Biointerfaces*, vol. 34, no. 3, pp. 173–177, 2004.
- [43] A. Syahir, K. Usui, K.-y. Tomizaki, K. Kajikawa, and H. Mihara, “Label and label-free detection techniques for protein microarrays,” *Microarrays*, vol. 4, no. 2, pp. 228–244, 2015.
- [44] D. G. Myszka, “Kinetic, equilibrium, and thermodynamic analysis of macromolecular interactions with BIACORE,” in *Methods in Enzymology*, vol. 323, pp. 325–340, Elsevier, 2000.
- [45] N. Bhalla, S. Sathish, C. J. Galvin, R. A. Campbell, A. Sinha, and A. Q. Shen, “Plasma-assisted large-scale nanoassembly of metal–insulator bioplasmonic mushrooms,” *ACS Applied Materials & Interfaces*, vol. 10, no. 1, pp. 219–226, 2018.
- [46] N. Bhalla, S. Sathish, A. Sinha, and A. Q. Shen, “Large-scale nanophotonic structures for long-term monitoring of cell proliferation,” *Advanced Biosystems*, vol. 2, no. 4, p. 1700258, 2018.
- [47] M. Pohanka, “The piezoelectric biosensors: principles and applications,” *International Journal of Electrochemical Science*, vol. 12, pp. 496–506, 2017.
- [48] R. Funari, B. Della Ventura, L. Schiavo, R. Esposito, C. Altucci, and R. Velotta, “Detection of parathion pesticide by quartz crystal microbalance functionalized with UV-activated antibodies,” *Analytical Chemistry*, vol. 85, no. 13, pp. 6392–6397, 2013.
- [49] C. V. Sapan, R. L. Lundblad, and N. C. Price, “Colorimetric protein assay techniques,” *Biotechnology and Applied Biochemistry*, vol. 29, no. 2, pp. 99–108, 1999.

-
- [50] J. M. Hicks, "Fluorescence immunoassay," *Human Pathology*, vol. 15, no. 2, pp. 112–116, 1984.
- [51] A. Sharma and S. G. Schulman, *Introduction to fluorescence spectroscopy*, vol. 13. Wiley New York, 1999.
- [52] R. P. Ekins and F. Chu, "Multianalyte microspot immunoassay—microanalytical "compact disk" of the future.," *Clinical Chemistry*, vol. 37, no. 11, pp. 1955–1967, 1991.
- [53] A. Sadeghi, Y. Amini, M. H. Saidi, and S. Chakraborty, "Numerical modeling of surface reaction kinetics in electrokinetically actuated microfluidic devices," *Analytica Chimica Acta*, vol. 838, pp. 64–75, 2014.
- [54] N. S. Lynn, H. Šípová, P. Adam, and J. Homola, "Enhancement of affinity-based biosensors: effect of sensing chamber geometry on sensitivity," *Lab on a Chip*, vol. 13, no. 7, pp. 1413–1421, 2013.
- [55] D. E. Rosner, "Convective diffusion limitations on the rates of chemical reactions at solid surfaces—kinetic implications," in *Symposium (International) on Combustion*, vol. 11, pp. 181–196, Elsevier, 1967.
- [56] H. Parsa, C. D. Chin, P. Mongkolwisetwara, B. W. Lee, J. J. Wang, and S. K. Sia, "Effect of volume- and time-based constraints on capture of analytes in microfluidic heterogeneous immunoassays," *Lab on a Chip*, vol. 8, no. 12, pp. 2062–2070, 2008.
- [57] C. J. Galvin, K. Shirai, A. Rahmani, K. Masaya, and A. Q. Shen, "Total capture, convection-limited nanofluidic immunoassays exhibiting nanoconfinement effects," *Analytical Chemistry*, vol. 90, no. 5, pp. 3211–3219, 2018.
- [58] T. Gervais and K. F. Jensen, "Mass transport and surface reactions in microfluidic systems," *Chemical Engineering Science*, vol. 61, no. 4, pp. 1102–1121, 2006.
- [59] T. M. Squires, R. J. Messinger, and S. R. Manalis, "Making it stick: convection, reaction and diffusion in surface-based biosensors," *Nature Biotechnology*, vol. 26, no. 4, pp. 417–426, 2008.
- [60] D. C. Prasher, V. K. Eckenrode, W. W. Ward, F. G. Prendergast, and M. J. Cormier, "Primary structure of the *Aequorea victoria* green-fluorescent protein," *Gene*, vol. 111, no. 2, pp. 229–233, 1992.
- [61] D. E. Crone, Y.-M. Huang, D. J. Pitman, C. Schenkelberg, K. Fraser, S. Macari, and C. Bystroff, "GFP-based biosensors," in *State of the Art in Biosensors-General Aspects*, IntechOpen, 2013.
- [62] D. Wild, *The immunoassay handbook: theory and applications of ligand binding, ELISA and related techniques*. Elsevier, 2013.
- [63] D. Baud, L. Regan, and G. Greub, "Comparison of five commercial serological tests for the detection of anti-*Chlamydia trachomatis* antibodies," *European Journal of Clinical Microbiology & Infectious Diseases*, vol. 29, no. 6, pp. 669–675, 2010.

- [64] C. Jones, P. Maple, N. Andrews, I. Paul, and E. Caul, "Measurement of IgG antibodies to *Chlamydia trachomatis* by commercial enzyme immunoassays and immunofluorescence in sera from pregnant women and patients with infertility, pelvic inflammatory disease, ectopic pregnancy, and laboratory diagnosed chlamydia psittaci/chlamydia pneumoniae infection," *Journal of Clinical Pathology*, vol. 56, no. 3, pp. 225–229, 2003.
- [65] C. Bax, J. Mutsaers, C. Jansen, J. Trimbos, P. Dörr, and P. Oostvogel, "Comparison of serological assays for detection of *Chlamydia trachomatis* antibodies in different groups of obstetrical and gynecological patients," *Clinical and Diagnostic Laboratory Immunology*, vol. 10, no. 1, pp. 174–176, 2003.
- [66] J. S. Yudkin, M. Kumari, S. E. Humphries, and V. Mohamed-Ali, "Inflammation, obesity, stress and coronary heart disease: is interleukin-6 the link?," *Atherosclerosis*, vol. 148, no. 2, pp. 209–214, 2000.
- [67] A. G. Vos, N. S. Idris, R. E. Barth, K. Klipstein-Grobusch, and D. E. Grobbee, "Pro-inflammatory markers in relation to cardiovascular disease in HIV infection. a systematic review," *PloS One*, vol. 11, no. 1, p. e0147484, 2016.
- [68] I. Kushner, "C-reactive protein and atherosclerosis," *Science*, vol. 297, no. 5581, pp. 520–521, 2002.
- [69] P. M. Ridker, "Clinical application of c-reactive protein for cardiovascular disease detection and prevention," *Circulation*, vol. 107, no. 3, pp. 363–369, 2003.
- [70] S. K. Vashist, A. Venkatesh, E. M. Schneider, C. Beaudoin, P. B. Luppa, and J. H. Luong, "Bioanalytical advances in assays for c-reactive protein," *Biotechnology Advances*, vol. 34, no. 3, pp. 272–290, 2016.
- [71] I. Pereiro, A. Fomitcheva-Khartchenko, and G. V. Kaigala, "Shake it or shrink it: Mass transport and kinetics in surface bioassays using agitation and microfluidics," *Analytical Chemistry*, vol. 92, no. 15, p. 10187–10195, 2020.
- [72] M. Selmi, M. H. Gazzah, and H. Belmabrouk, "Optimization of microfluidic biosensor efficiency by means of fluid flow engineering," *Scientific Reports*, vol. 7, no. 1, pp. 1–11, 2017.
- [73] B. E. Rapp, *Microfluidics: modeling, mechanics and mathematics*. William Andrew, 2016.
- [74] D. Gelinsky-Wersing, W. Wersing, and W. Pompe, "Bivalent kinetic binding model to surface plasmon resonance studies of antigen-antibody displacement reactions," *Analytical Biochemistry*, vol. 518, pp. 110–125, 2017.
- [75] T. Palmer and P. L. Bonner, *Enzymes: biochemistry, biotechnology, clinical chemistry*. Elsevier, 2007.

-
- [76] D. J. O'Shannessy, "Determination of kinetic rate and equilibrium binding constants for macromolecular interactions: a critique of the surface plasmon resonance literature," *Current Opinion in Biotechnology*, vol. 5, no. 1, pp. 65–71, 1994.
- [77] M. Tanaka, G. Girard, R. Davis, A. Peuto, and N. Bignell, "Recommended table for the density of water between 0 c and 40 c based on recent experimental reports," *Metrologia*, vol. 38, no. 4, p. 301, 2001.
- [78] L. Korson, W. Drost-Hansen, and F. J. Millero, "Viscosity of water at various temperatures," *The Journal of Physical Chemistry*, vol. 73, no. 1, pp. 34–39, 1969.
- [79] K. Burczak, T. Fujisato, M. Hatada, and Y. Ikada, "Protein permeation through poly (vinyl alcohol) hydrogel membranes," *Biomaterials*, vol. 15, no. 3, pp. 231–238, 1994.
- [80] C. Chou, H.-Y. Hsu, H.-T. Wu, K.-Y. Tseng, A. E. Chiou, C.-J. Yu, Z.-Y. Lee, and T.-S. Chan, "Fiber optic biosensor for the detection of c-reactive protein and the study of protein binding kinetics," *Journal of Biomedical Optics*, vol. 12, no. 2, p. 024025, 2007.
- [81] C.-K. Yang, J.-S. Chang, S. D. Chao, and K.-C. Wu, "Effects of diffusion boundary layer on reaction kinetics of immunoassay in a biosensor," *Journal of Applied Physics*, vol. 103, no. 8, p. 084702, 2008.
- [82] F. M. White and I. Corfield, *Viscous fluid flow, Vol. 2*. McGraw-Hill, New York, 1991.
- [83] A. Shrivastava and V. B. Gupta, "Methods for the determination of limit of detection and limit of quantitation of the analytical methods," *Chronicles of Young Scientists*, vol. 2, no. 1, pp. 21–25, 2011.
- [84] S. Chen and T. A. Springer, "Selectin receptor–ligand bonds: Formation limited by shear rate and dissociation governed by the Bell model," *Proceedings of the National Academy of Sciences*, vol. 98, no. 3, pp. 950–955, 2001.
- [85] V. Ramachandran, T. Yago, T. K. Epperson, M. M. Kobzdej, M. U. Nollert, R. D. Cummings, C. Zhu, and R. P. McEver, "Dimerization of a selectin and its ligand stabilizes cell rolling and enhances tether strength in shear flow," *Proceedings of the National Academy of Sciences*, vol. 98, no. 18, pp. 10166–10171, 2001.
- [86] A. A. Kortt, E. Nice, and L. C. Gruen, "Analysis of the binding of the Fab fragment of monoclonal antibody NC10 to influenza virus N9 neuraminidase from tern and whale using the BIAcore biosensor: effect of immobilization level and flow rate on kinetic analysis," *Analytical Biochemistry*, vol. 273, no. 1, pp. 133–141, 1999.
- [87] G. A. Canziani, S. Klakamp, and D. G. Myszk, "Kinetic screening of antibodies from crude hybridoma samples using Biacore," *Analytical Biochemistry*, vol. 325, no. 2, pp. 301–307, 2004.

- [88] J. M. Leth and M. Ploug, “Determination of binding kinetics of intrinsically disordered proteins by surface plasmon resonance,” in *Intrinsically Disordered Proteins*, pp. 611–627, Springer, 2020.